Dalton Transactions c4dt03210a

1

Gold nanoparticles functionalised with fast water exchanging Gd^{3+} chelates: linker effects on the relaxivity

Miguel F. Ferreira, Janaina Gonçalves, B. Mousavi, M. I. M. Prata, S. P. J. Rodrigues, Daniel Calle, Pilar López-Larrubia, Sebastian Cerdan, Tiago B. Rodrigues, Paula M. Ferreira, L. Helm,* José A. Martins* and Carlos F. G. C. Geraldes

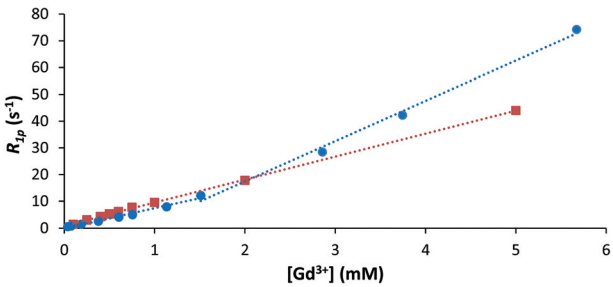

The relaxivity displayed by Gd^{3+} chelates immobilized onto gold nanoparticles is the result of the complex interplay between the nanoparticle size, the water exchange rate and the chelate structure.

Q4 Q3

Please check this proof carefully. **Our staff will not read it in detail after you have returned it.**

Translation errors between word-processor files and typesetting systems can occur so the whole proof needs to be read. Please pay particular attention to: tabulated material; equations; numerical data; figures and graphics; and references. If you have not already indicated the corresponding author(s) please mark their name(s) with an asterisk. Please e-mail a list of corrections or the PDF with electronic notes attached – do not change the text within the PDF file or send a revised manuscript. Corrections at this stage should be minor and not involve extensive changes. All corrections must be sent at the same time.

Please bear in mind that minor layout improvements, e.g. in line breaking, table widths and graphic placement, are routinely applied to the final version.

We will publish articles on the web as soon as possible after receiving your corrections; **no late corrections will be made**.

Please return your **final** corrections, where possible within **48 hours** of receipt, by e-mail to: dalton@rsc.org

Queries for the attention of the authors

Journal: **Dalton Transactions**

Paper: **c4dt03210a**

Title: **Gold nanoparticles functionalised with fast water exchanging Gd^{3+} chelates: linker effects on the relaxivity**

Editor's queries are marked like this [Q1, Q2, ...], and for your convenience line numbers are indicated like this [5, 10, 15, ...].

Please ensure that all queries are answered when returning your proof corrections so that publication of your article is not delayed.

Query Reference	Query	Remarks
Q1	For your information: You can cite this article before you receive notification of the page numbers by using the following format: (authors), Dalton Trans., (year), DOI: 10.1039/c4dt03210a.	
Q2	Please carefully check the spelling of all author names. This is important for the correct indexing and future citation of your article. No late corrections can be made.	
Q3	Please check that the inserted GA image is suitable.	
Q4	The first line of the abstract has been inserted as the GA text. Please check that this is suitable. If the text does not fit within the two horizontal lines, please trim the text and/or the title.	
Q5	The meaning of the sentence beginning "The selective enhancement..." is not clear - please clarify.	
Q6	As Fig. 5 and associated caption were not supplied, we have changed Fig. 6 to Fig. 5 and renumbered all of the subsequent figures accordingly. Please check that the renumbering is correct and that all of the citations within the text correspond to the correct figure, and indicate any changes required.	
Q7	Ref. 39: Please provide the year of publication.	

Dalton Transactions

PAPER

Gold nanoparticles functionalised with fast water exchanging Gd^{3+} chelates: linker effects on the relaxivity†

Cite this: DOI: 10.1039/c4dt03210a

Miguel F. Ferreira,[a] Janaina Gonçalves,[a] B. Mousavi,[b] M. I. M. Prata,[c] S. P. J. Rodrigues,[d] Daniel Calle,[e] Pilar López-Larrubia,[e] Sebastian Cerdan,[e] Tiago B. Rodrigues,[f,g] Paula M. Ferreira,[a] L. Helm,*[b] José A. Martins*[a] and Carlos F. G. C. Geraldes[h]

Received 17th October 2014,
Accepted 7th January 2015

DOI: 10.1039/c4dt03210a

www.rsc.org/dalton

The relaxivity displayed by Gd^{3+} chelates immobilized onto gold nanoparticles is the result of the complex interplay between the nanoparticle size, the water exchange rate and the chelate structure. In this work we study the effect of the length of ω-thioalkyl linkers, anchoring fast water exchanging Gd^{3+} chelates onto gold nanoparticles, on the relaxivity of the immobilized chelates. Gold nanoparticles functionalized with Gd^{3+} chelates of mercaptoundecanoyl and lipoyl amide conjugates of the DO3A-*N*-(α-amino)propionate chelator were prepared and studied as potential CA for MRI. High relaxivities per chelate, of the order of magnitude 28–38 mM^{-1} s^{-1} (30 MHz, 25 °C), were attained thanks to simultaneous optimization of the rotational correlation time and of the water exchange rate. Fast local rotational motions of the immobilized chelates around connecting linkers (internal flexibility) still limit the attainable relaxivity. The degree of internal flexibility of the immobilized chelates seems not to be correlated with the length of the connecting linkers. Biodistribution and MRI studies in mice suggest that the *in vivo* behavior of the gold nanoparticles was determined mainly by size. Small nanoparticles (HD = 3.9 nm) undergo fast renal clearance and avoidance of the RES organs while larger nanoparticles (HD = 4.8 nm) undergo predominantly hepatobiliary excretion. High relaxivities, allied to chelate and nanoparticle stability and fast renal clearance *in vivo* suggest that functionalized gold nanoparticles hold great potential for further investigation as MRI contrast agents. This study contributes to a better understanding of the effect of linker length on the relaxivity of gold nanoparticles functionalized with Gd^{3+} complexes. It is a relevant contribution towards "design rules" for nanostructures functionalized with Gd^{3+} chelates as Contrast Agents for MRI and multimodal imaging.

Introduction

MRI is becoming the "central imaging modality" in clinical diagnostics.[1] MRI is based on the nuclear magnetic resonance phenomenon (NMR). In MRI scans, essentially, the relaxation times (T_1 and T_2) of the water protons of tissues (intrinsically different) are acquired and reconstructed into three-dimensional anatomical images.[2,3] MRI is inherently non-invasive, makes use of (benign) non-ionizing radiation (static and radiofrequency magnetic fields), is depth independent and displays superb spatial resolution. Low detection sensitivity (inherent to the NMR phenomenon) is the main limitation of MRI.[4] Contrast agents (CA) are paramagnetic species (Gd^{3+}, Mn^{2+}, Fe^{3+}, stable organic radicals, iron oxide nanoparticles, *etc.*) that by promoting selective reduction of T_1 or T_2 of the water protons of tissues can generate dramatic contrast enhancements.[5,6] The selective enhancement of the relaxation rates, $R_{1,2}$ ($R_{1,2}$ =

[a]Centro de Química, Campus de Gualtar, Universidade do Minho, 4710-057 Braga, Portugal. E-mail: jmartins@quimica.uminho.pt
[b]Laboratoire de Chimie Inorganique et Bioinorganique, Ecole Polytechnique Fédérale de Lausanne, EPFL-BCH CH-1015, Lausanne, Switzerland.
E-mail: lothar.helm@epfl.ch; Fax: +41 (0)21 693 98 95; Tel: +41 (0)21 693 98 76
[c]IBILI and ICNAS, Universidade de Coimbra, Coimbra, Portugal
[d]Chemistry Center and Department of Chemistry, University of Coimbra, 3004-535 Coimbra, Portugal
[e]Instituto de Investigaciones Biomédicas "Alberto Sols", CSIC-UAM, Madrid, Spain
[f]Cancer Research UK Cambridge Research Institute, Li KaShing Centre, Cambridge CB2 0RE, UK
[g]Department of Biochemistry, University of Cambridge, Cambridge CB2 1GA, UK
[h]Chemistry Center and Department of Life Sciences, Faculty of Science and Technology, University of Coimbra, Calçada Martim de Freitas, 3000-393 Coimbra, Portugal

†Electronic supplementary information (ESI) available. See DOI: 10.1039/c4dt03210a

$1/T_{1,2}$), normalized to 1 mM concentration of paramagnetic centres – relaxivity ($r_{1,2}$, units: mM^{-1} s^{-1}), measures CA efficacy.[4,7] Approved CA for clinical MRI are either Gd^{3+} complexes with linear (DTPA-type) and macrocyclic (DOTA-type) poly(aminocarboxylate) ligands (T_1-weighed MRI)[8] or iron oxide nanoparticles (IONPS) stabilized with dextran (T_2–T_2*-weighed MRI).[9] Low molecular weight Gd^{3+}-based CA display relaxivities of the order of magnitude 3–5 mM^{-1} s^{-1} at magnetic fields relevant (currently) for clinical MRI (20–120 MHz). The Solomon–Bloembergen–Morgan (SBM) theory predicts that very high relaxivities, of the order of magnitude 100 mM^{-1} s^{-1} at magnetic fields relevant for clinical imaging (20–120 MHz), are attainable by Gd^{3+} chelates displaying simultaneous optimization of the main parameters that govern relaxivity: rotational correlation times (τ_R), water exchange rate constant (k_{ex}) and electron relaxation parameters (τ_v and Δ^2).[4,7] Despite great advancements in the design and synthesis of CA during the past two decades, the ideal CA displaying very high relaxivity and safety *in vivo*, a targeting capability and responsiveness coupled to therapeutic properties is still elusive.[10]

The "nanotechnology revolution" is underway with a dramatic impact in many fields, particularly in medical imaging.[11] Gold nanostructures (nanoparticles, nanoclusters, nanorods, *etc.*) have found many applications in chemistry, medicine, biotechnology, and other fields owing to intrinsic reporting properties (localized surface plasmon resonance, fluorescence, and X-ray attenuation)[12] coupled to therapeutic properties (hyperthermia and X-ray sensitization),[13] biocompatibility and safety *in vivo*[14] and facile preparation with tunable size and surface properties by bottom-up methodologies.[15] The first generation of gold nanoparticles (AuNPs) CA made use of easy to synthesize, thiol-functionalised Gd(DTPA-bis-amide)[16–18] and Gd(DO3A)-type chelates.[19] Superb relaxivities (per nanoparticle) were attained thanks to chelate clustering.[16] *In vivo* MRI studies established the merits of AuNPs as CA for MRI, bimodal MRI/X-ray imaging and as theragnostics (MRI/X-ray sensitization).[16–18,20] Slow water exchange and fast local rotational motions of the immobilized chelates around linkers/spacers (chelate flexibility) result in relaxivity enhancements (per chelate) lower than those expected for Gd^{3+} chelates appended to rigid nanosized objects.[16–18,21,22] Helm and co-workers reported very high relaxivity per chelate immobilized onto AuNPs (60 mM^{-1} s^{-1}; 30 MHz, 25 °C), attributed to two exchanging inner sphere water molecules in Gd(DTTA)-type chelates and complete rigidity of the chelates immobilized *via* a short aromatic linker.[23] The relaxivity was, however, still limited by slow water exchange. We have demonstrated in previous studies that the Gd[DO3A-*N*-(α-amino)propionate] chelate and Gd^{3+} complexes of amide conjugates of the DO3A-*N*-(α-amino)propionate chelator display water exchange rates within the range considered ideal for attaining high relaxivities at intermediate fields, thanks to "steric compression around the water binding site".[24–26] AuNPs functionalized with the fast water exchanging chelate Gd[DO3A-*N*-(α-cystamido)propionate] display high relaxivities at intermediate and high fields (27 and 8.0 mM^{-1} s^{-1}; 20 and 200 MHz, respectively, 25 °C) as a result of simultaneous optimization of the rotational dynamics and water exchange rate.[27] Fast local rotational motions around the cysteine linker still limit the attainable relaxivity, as demonstrated before for other macromolecular/nanosized objects such as micelles, dendrimers, polymers, *etc.*[26–28] In this work we address the effect of the length of the ω-thioalkyl linker, anchoring fast water exchanging Gd[DO3A-*N*-(α-amido)propionate] chelates to gold nanoparticles, on the relaxivity. Biodistribution and *in vivo* MRI studies with the functionalized AuNPs as CA are also reported.

Synthesis and characterization

Mercaptoundecanoyl and lipoyl conjugates of the DO3A-*N*-(α-amino)propionate chelator were synthesized to study the effect of the length of the ω-thioalkyl linker on the relaxivity of AuNPs functionalized with Gd^{3+} chelates (Scheme 1).

The lipoic acid conjugate (**L_1**) was prepared following the synthetic methodology reported before for the cysteine conjugate of the DO3A-*N*-(α-amino)propionate chelator (**L_3**).[27] The synthetic pathway excludes, all along, acidic conditions likely to promote oligomerization of the chelator through the lipoic acid moiety.[29] Deprotection of the fully alkylated orthogonally protected intermediate **6** allows direct conjugation of lipoic acid to the preformed DO3A-*N*-α-(amino)propionate scaffold.[27] For preparing the 11-mercaptoundecanoyl conjugate (**L_2**) the preformed amide was introduced into the *cyclen* scaffold *via* Michael addition of the *N*-Boc,*N*-(11-(acetylthio)undecanoyl)-dehydroalanine methyl ester electrophile (**3**).[25,26] Reactive block **3** was prepared over 3 steps in 48% overall yield (Scheme 2).[30]

The thioacetyl protecting group has proved easy to install and stable under mild alkaline and strong acidic conditions *en route* to **L_2**. The final deprotection was performed in one step by saponification with ethanolic NaOH. Following pH adjustment to neutrality with diluted hydrochloric acid, chelators **L_1** and **L_2** were adsorbed onto silica and purified by flash chromatography followed by size exclusion chromatography (SEC) on Sephadex G10 with water elution.

Relaxometric studies of GdL_1 and GdL_2

The concentration dependence of the paramagnetic longitudinal water proton relaxation rate (R_{1p}) was measured for Gd**L_1** and Gd**L_2** (20 MHz, 25 °C, pH 7.1) (Fig. 1).

The relaxation rate data for Gd**L_1** can be well fitted to a straight line (eqn (1)) affording a relaxivity of 8.6 ± 0.9 mM^{-1} s^{-1} (20 MHz, 25 °C, pH 7.1), characteristic of low/intermediate molecular weight chelates in fast rotation in solution. Fitting the relaxation rate data of Gd**L_2** requires two straight lines with different slopes (eqn (1) and (2)). The concentration at the interception of the two lines defines the critical micelle concentration, cmc (cmc = 1.5 ± 0.3 mM).[31]

$$R_{1p} = R_1^{obs} - R_1^{d} = r_1^{na} \times C_{Gd} \quad (1)$$

$$R_{1p} = R_1^{obs} - R_1^{d} = (r_1^{na} - r_1^{a})\text{cmc} + r_1^{a} \times C_{Gd} \quad (2)$$

R_1^{obs} is the longitudinal relaxation rate measured for the solution, R_1^{d} is the diamagnetic contribution to the

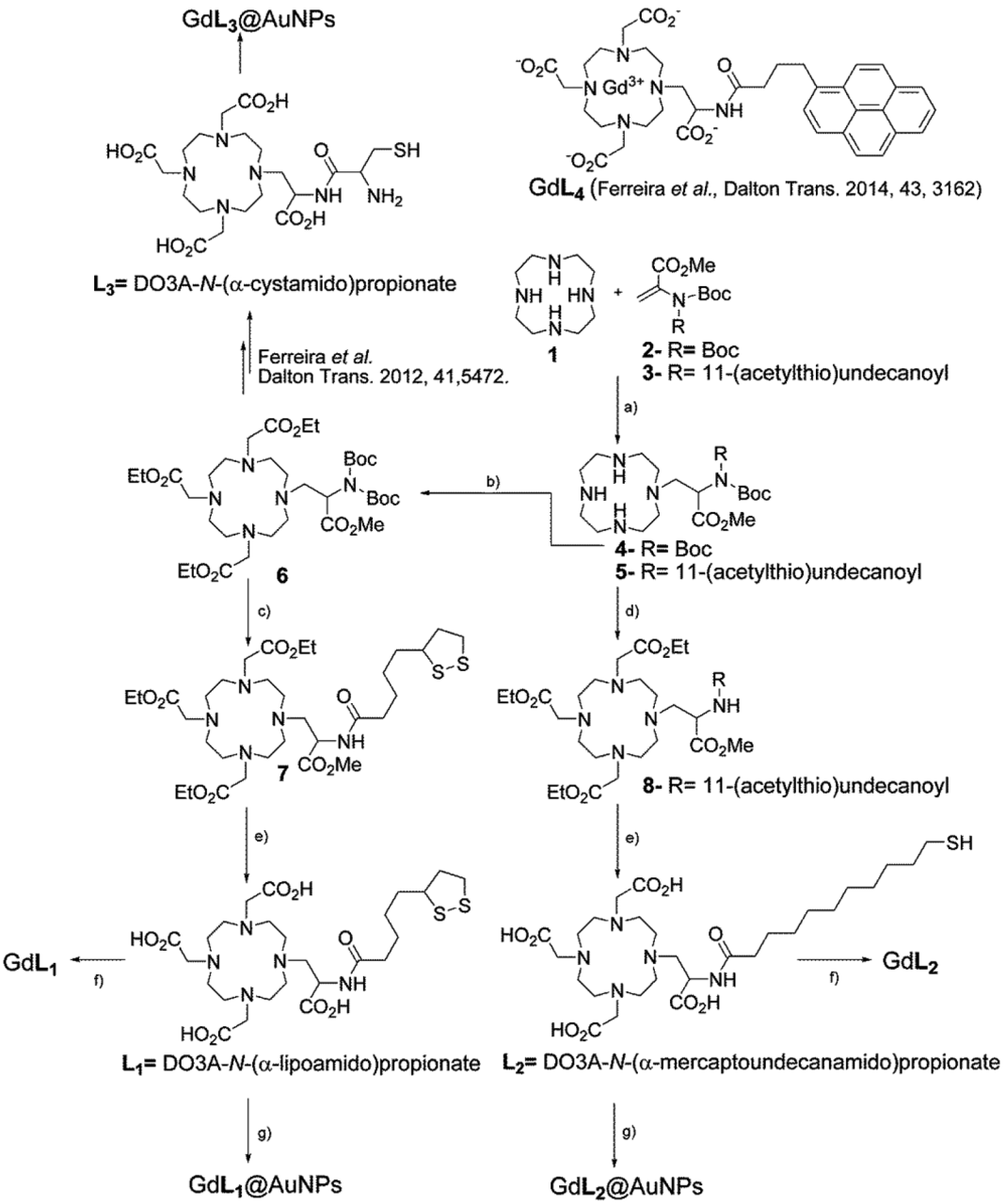

Scheme 1 Synthetic pathway for ω-thioalkyl conjugates of the DO3A-*N*-(α-amino)propionate chelator: (a) K_2CO_3/MeCN; (b) ethyl bromoacetate, K_2CO_3/MeCN; (c) i. TFA/CH_2Cl_2, ii. DIPEA/CH_2Cl_2, lipoic acid, DCC/HOBt; (d) i) TFA/DCM, ii. Ethyl bromoacetate, K_2CO_3/MeCN; (e) i. NaOH aq., ii. Flash chromatography silica gel, iii. SEM (Sephadex G10); (f) $GdCl_3{\cdot}6H_2O$; (g) i. $HAuCl_4$, $NaBH_4$, ii. $GdCl_3{\cdot}6H_2O$, iii. SEM (Sephadex G10) followed by dialysis (cellulose tubing MWCO 10 kDa).

longitudinal relaxation rate (the relaxation rate of pure water), and C_{Gd} is the analytical Gd^{3+} concentration.

Below the cmc, Gd**L**$_2$ is present in solution as monomers (non-aggregated), displaying a relaxivity (r_1^{na} = 6.6 ± 0.1 mM^{-1} s^{-1}; 20 MHz, 25 °C, pH 7.1) characteristic of low molecular weight chelates (eqn (1)).

For Gd**L**$_2$ at concentrations above the cmc the relaxation rate has a contribution from monomers (at a concentration equal to the cmc value) and from the (aggregated) micellar form (r_1^{a} = 15.1 ± 0.8 mM^{-1} s^{-1}; 20 MHz, 25 °C, pH 7.1) (eqn. (2)). Self-association of Gd**L**$_2$ into micelle-type structures leads to an increase of the effective molecular volume of the chelate. Slow tumbling in solution (longer rotational correlation times) translates into substantially higher relaxivity for the aggregated form of Gd**L**$_2$ compared to its monomeric (non-aggregated) form. The relaxivity enhancement for Gd**L**$_2$ upon self-assembly is of the same order of magnitude as that reported for the DOTA-type Gd(DOTASA-C12) chelate functionalized with a C_{12} alkyl chain (r_1^{a} = 18.0 mM^{-1} s^{-1}, 20 MHz, 25 °C),[32] but significantly lower than that attained by the aggregated form of the

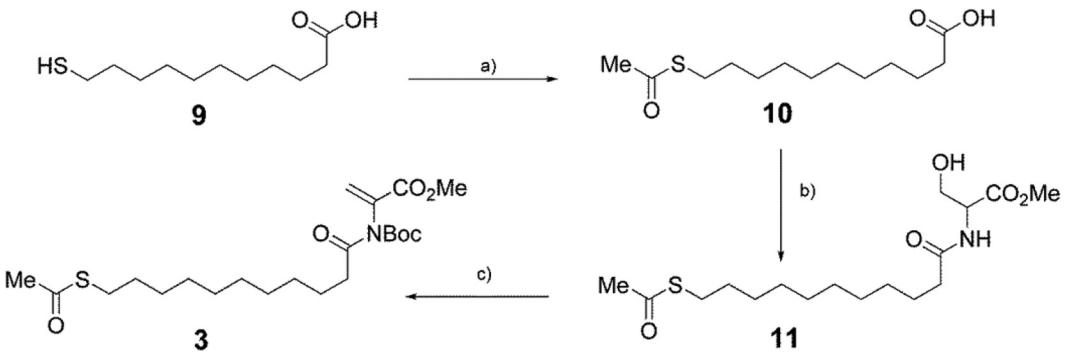

Scheme 2 Synthetic route for Michael electrophile *N*-Boc,*N*-(11-(acetylthio)undecanoyl)dehydroalanine methyl ester (**3**): (a) acetic anhydride/pyridine; (b) serine methyl ester hydrochloride, HOBt/DCC/NEt_3; (c) Boc_2O/DMAP, dry acetonitrile.

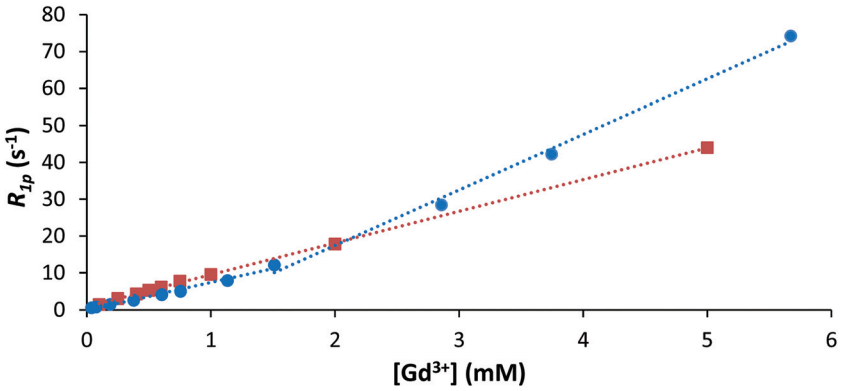

Fig. 1 Concentration dependence of the paramagnetic water proton relaxation rate R_{1p} = (R_1^{obs}–R_{1d}) for GdL_1 (■) and GdL_2 (●) (20 MHz, 25 °C, pH 7.1).

fast water exchanging Gd[DO3A-*N*-(α-pyrenebutanamido)propionate] chelate (Gd$\mathbf{L_4}$ in Scheme 1) (r_1^a = 32 mM^{-1} s^{-1}; 20 MHz; 25 °C).[26] The temperature dependence of the water proton longitudinal relaxation rate for Gd$\mathbf{L_1}$ and Gd$\mathbf{L_2}$ (20 MHz, 25 °C) (Fig. SI1†) indicates that the relaxivity is not limited by slow water exchange, as demonstrated before for other Gd^{3+} chelates of amide conjugates of the DO3A-*N*-(α-amino)propionate chelator.[24,27] As both Gd$\mathbf{L_2}$ and Gd[DO3A-*N*-(α-pyrenebutanamido)propionate] chelates display fast water exchange, the lower relaxivity attained by Gd$\mathbf{L_2}$ has to be ascribed to higher internal flexibility and/or smaller size of the Gd$\mathbf{L_2}$ micelles (Fig. SI2†). The pH dependence of the proton relaxation rate (Fig. SI3†) and the transmetallation study (Fig. SI4†) show that Gd$\mathbf{L_1}$ and Gd$\mathbf{L_2}$ are stable in the physiological pH range and kinetically inert towards transmetallation against Zn^{2+}.[33]

Preparation of gold nanoparticles functionalized with Gd$\mathbf{L_1}$ and Gd$\mathbf{L_2}$ chelates

A modified Brust's methodology in aqueous solution was employed for preparing AuNPs functionalized with Gd$\mathbf{L_1}$ and Gd$\mathbf{L_2}$ chelates.[27,34] Using directly the Gd$\mathbf{L_1}$ and Gd$\mathbf{L_2}$ chelates as nanoparticle stabilizers resulted in extensive precipitation upon addition of the reducing agent ($NaBH_4$). Attempts to functionalize citrate-stabilized AuNPs with Gd$\mathbf{L_1}$ and Gd$\mathbf{L_2}$ chelates *via* place exchange was also revealed to be unsuccessful.[18] A two-step methodology, using the $\mathbf{L_1}$ and $\mathbf{L_2}$ chelators as NPs stabilizers, followed by Gd^{3+} complexation, was revealed to be successful for preparing AuNPs functionalized with Gd$\mathbf{L_1}$ and Gd$\mathbf{L_2}$ chelates (Scheme 1).[27]

Solutions containing equimolar amounts of $\mathbf{L_1}$ or $\mathbf{L_2}$ and $HAuCl_4$ turned immediately dark brown upon addition, in one aliquot, of one molar equivalent of $NaBH_4$. Adding a molar equivalent of Gd^{3+}, in relation to the total amount of $\mathbf{L_1}$ or $\mathbf{L_2}$ in the crude mixture, resulted in stable NPs. Size exclusion chromatography (SEC) (Sephadex G10, elution with water) followed by extensive dialysis against water (cellulose tubing MWCO 10 000) afforded stable AuNPs functionalized with Gd$\mathbf{L_1}$ and Gd$\mathbf{L_2}$ chelates. A single fraction, including the broad colored band eluting on SEC, was collected. The absence of (free) uncomplexed Gd^{3+} was confirmed by the xylenol orange test.[35]

Characterization of Gd$\mathbf{L_1}$@AuNPs and Gd$\mathbf{L_2}$@AuNPs preparation

The Gd content of the functionalized AuNPs was estimated by bulk magnetic susceptibility measurements[36] and further confirmed by ICP-OES following sample digestion with *aqua regia* (HCl/HNO_3; 3/1, v/v) (Table 1).[27,37]

Table 1 Characterization of GdL_1@AuNPs and GdL_2@AuNPs

	GdL_1@AuNPs[a]	GdL_2@AuNPs[a]	GdL_3@AuNPs[b]
[Gd] (mM)[c]	0.57	1.30	1.24
HD (nm)[d]	4.8	5.9	3.9
Zeta-potential (mV)	−6.3	−13,7	−12.3
D_{Au}[e]	1.0	0.9	0.7[f]

[a] This work. [b] Ref. 27. [c] Determined by ICP-OES. [d] DLS measurements. [e] Estimated from the HD and semi-empirical calculations of the chelate monolayer thickness – see Table SI2. [f] Revised value according to semi-empirical calculations for the length of Gd$\mathbf{L_3}$.

The AuNPs were characterized regarding size distribution by Dynamic Light Scattering (DLS) (Fig. 2) and Transmission Electron Microscopy (TEM) (Fig. 3).

DLS measurements give the hydrodynamic diameter (HD) of NPs, including the Au nanocrystal core, the chelate monolayer and the immobile ionic layer surrounding the NPs. An average HD of 4.8 nm (NPs distribution in the range 3–10 nm with a maximum at 3–4 nm) and 5.9 nm (NPs distribution in the range 2–11 nm with a maximum at 4–5 nm) was measured for Gd$\mathbf{L_1}$@AuNps and Gd$\mathbf{L_2}$@AuNPs, respectively. TEM measurements reveal only the nanocrystal core. The TEM images obtained for Gd$\mathbf{L_1}$@AuNPs and Gd$\mathbf{L_2}$@AuNPs do not allow determining the average diameter of the Au core owing to the very small size of the NPs. From the TEM images one can only conclude that most Gd$\mathbf{L_1}$@AuNPs and Gd$\mathbf{L_2}$@AuNPs have a nanocrystal core with a diameter below 2 nm. The average diameter of the Au core of Gd$\mathbf{L_1}$@AuNPs and Gd$\mathbf{L_2}$@AuNPs (~1.0 and 0.9 nm, respectively) was estimated from the DLS measurements taking into account the thickness of the chelate monolayer, calculated by PM6 semi-empirical calculations for the most likely conformations of Gd$\mathbf{L_1}$ and Gd$\mathbf{L_2}$ bonded to one or two Au atoms (1.9 and 2.5 nm, respectively) (Fig. SI5, Table SI2†).[23,24] The absence of a well-defined plasmon absorption band in the UV-Vis spectra of Gd$\mathbf{L_1}$@AuNPs and Gd$\mathbf{L_2}$@AuNPs (Fig. SI6 and SI7†) corroborates the very small size of the NPs core.[38]

As $\mathbf{L_1}$, $\mathbf{L_2}$ and $\mathbf{L_3}$ share the same coordination cage, the length of the linker defines the overall wedge-like geometry of the chelator. Shorter linkers originate bulkier thiol ligands. Ligand bulkiness increases in the series $\mathbf{L_3}$ > $\mathbf{L_1}$ > $\mathbf{L_2}$ (Fig. SI5†). Bulkier thiols are likely to terminate the growth of AuNPs earlier than less bulky ligands, resulting in AuNPs displaying smaller Au cores associated with higher surface curvature.[39] This correlation (D_{Au} = 1.0, 0.9 and 0.7 nm for Gd$\mathbf{L_1}$, Gd$\mathbf{L_2}$ and Gd$\mathbf{L_3}$@AuNPs) is followed roughly by $\mathbf{L_2}$ and $\mathbf{L_3}$. The discrepancy observed for $\mathbf{L_1}$ can be due to the different sulfur binding modes.

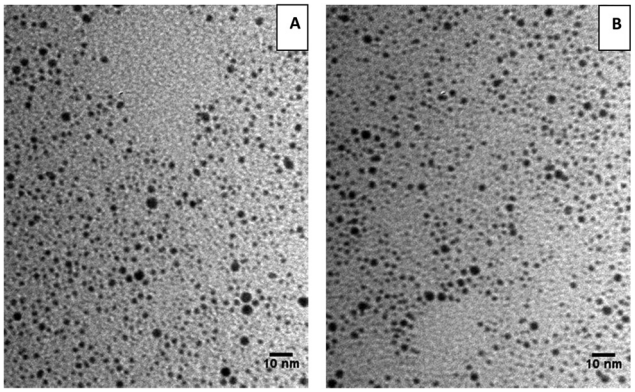

Fig. 3 Transmission electron microscopy (TEM) for Gd$\mathbf{L_1}$@AuNPs (**A**) and Gd$\mathbf{L_2}$@AuNPs (**B**).

Gd$\mathbf{L_1}$@AuNPs and Gd$\mathbf{L_2}$@AuNPs were found to be stable in solution for extended periods. The NPs could be freeze-dried and re-dissolved without aggregation/precipitation. This can be ascribed to the overall negative charge (−1) of the immobilized Gd^{3+} complexes, resulting in NPs displaying negative zeta-potential (Fig. SI8†).

Relaxometric characterization of GdL_1@AuNPs and GdL_2@AuNPs

The concentration dependence of the proton longitudinal relaxation rate (R_{1p}) was evaluated for Gd$\mathbf{L_1}$@AuNPs and Gd$\mathbf{L_2}$@AuNPs (r_1 = 29 and 38 mM^{-1} s^{-1}, respectively, 20 MHz, 25 °C, pH 7.1) (Fig. SI9†).

For relevant clinical applications chelates immobilized onto NPs must be stable regarding demetallation and inert towards transmetallation with physiological metal ions, mainly Zn^{2+}.[33] In addition to releasing toxic Gd^{3+}, demetallation and transmetallation processes of immobilized chelates are likely to trigger particle aggregation and precipitation *in vivo*. Stability

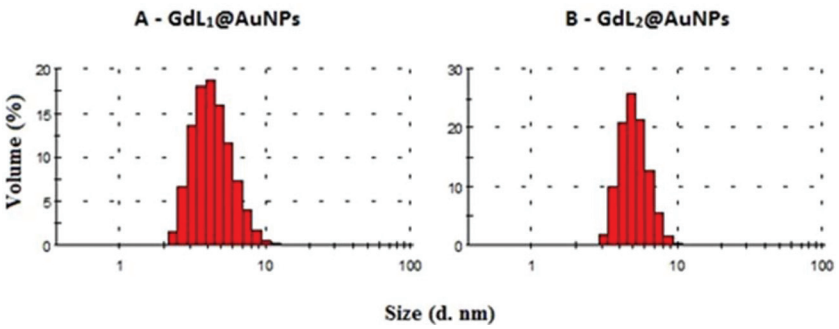

Fig. 2 Size distribution (% volume) for Gd$\mathbf{L_1}$@AuNPs (**A**) and Gd$\mathbf{L_2}$@AuNPs (**B**).

at low pH is particularly important as protonation-assisted mechanisms have been implicated in demetallation, presumably followed by transmetallation with serum ions, of macrocyclic Gd(DOTA)-type chelates.[33,40,41] The pH dependence of the protonic relaxation rate (R_{1p}) was evaluated for Gd**L**$_1$@AuNPs and Gd**L**$_2$@AuNPs in the pH range 3–10 (Fig. SI10†).

The kinetic stability of the immobilized chelates (and entire nanoparticles) was evaluated by challenging Gd**L**$_1$@AuNPs and Gd**L**$_2$@AuNPs with Zn^{2+} ions in phosphate buffer (Fig. SI11 and SI12†).[33] According to the criteria set by Muller and co-workers, the immobilized chelates (and whole NPs) can be classified as kinetically inert and thermodynamically stable.[33] The pH stability and kinetic inertness indicate that the NPs are potentially safe for *in vivo* applications.

Nuclear magnetic relaxation dispersion profiles

The magnetic field dependence of the proton relaxivity (r_1) (Nuclear Magnetic Relaxation Dispersion – NMRD profiles) was obtained for Gd**L**$_1$@AuNPs and Gd**L**$_2$@AuNPs in the Larmor frequency range 0.01–400 MHz. The most important parameters that govern relaxivity are the hydration number (q), the water exchange rate constant (k_{ex}), the rotational correlation time (τ_R) and the electron relaxation parameters (τ_v and Δ^2).[4,7] The number of water molecules in the first coordination sphere, the water exchange rate and the rotational correlation time can be tuned by chelate design. Clear rules to tune the electron relaxation parameters are still elusive.[42] Treating chelates immobilised onto macromolecular/nanosized objects (micelles, proteins, polymers, dendrimers, nanoparticles, viral particles) as rigid entities often fails to deliver reliable parameters from the fitting of the NMRD profiles to the SBM theory. In fact, it is necessary to assume in the fittings that the interactions that generate the relaxation are influenced by both fast local rotational motions (τ_{Rlocal}) of the immobilized chelates around linkers/spacers and a slower, global motion, common to the entire object ($\tau_{Rglobal}$). The degree of spatial restriction of the local motion (interpreted as chelate flexibility) is measured by the generalized, model independent order parameter – S^2. The order parameter can assume values in the range 0–1: $S^2 = 0$ if the internal motions are isotropic, and $S^2 = 1$ if the internal motions are completely restricted.[43]

In this work, it was assumed in the fittings that the immobilised Gd**L**$_1$ and Gd**L**$_2$ complexes have one inner sphere water molecule ($q = 1$) like other Gd^{3+} complexes of the DO_3A-*N*-(α-amino/amido)propionate family.[24–26] The water exchange rate constant and its activation enthalpy (k_{ex}^{298}, $\Delta H^{\ddagger}$) were fixed

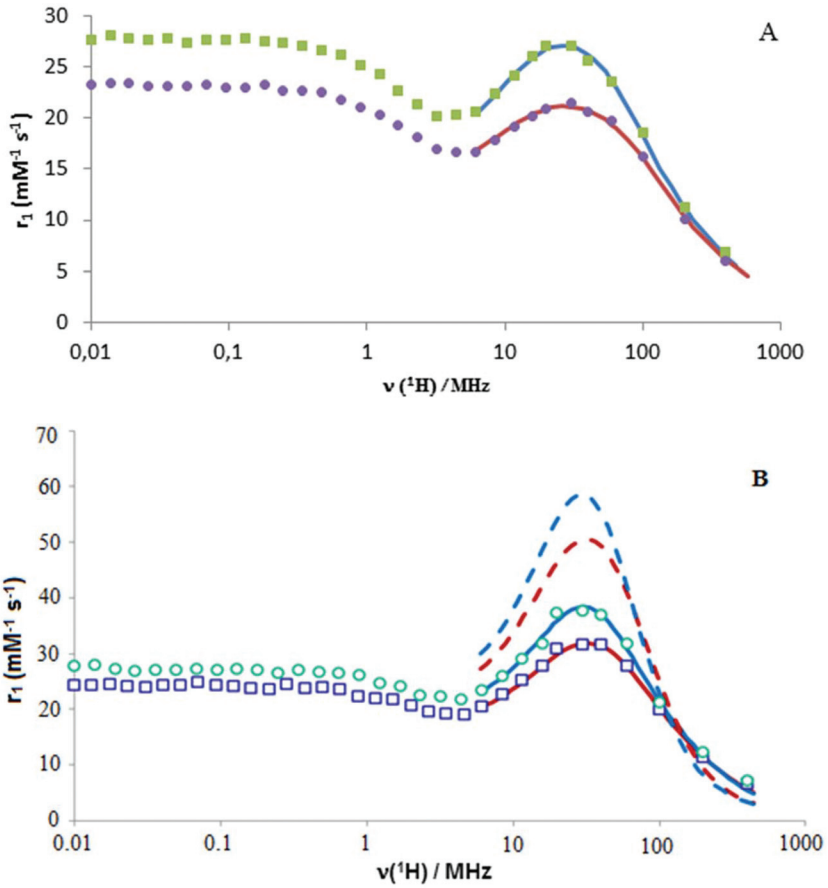

Fig. 4 ^{1}H Nuclear magnetic relaxation dispersion (NMRD) profiles for: A – Gd**L**$_1$@AuNPs (0.56 mM; pH 7.0); 25 °C (■) and 37 °C (●); B – Gd**L**$_2$@AuNPs (1.30 mM; pH 7.0); 25 °C (○) and 37 °C (□). The fitted curves are represented as continuous lines. The broken lines are the result of simulations using the same parameters as those in Table 2, but assuming total rigidity ($S^2 = 1$) of the immobilized chelates.

Table 2 Best fit parameters obtained for Gd$\mathbf{L_1}$@AuNPs and Gd$\mathbf{L_2}$@AuNPs from the fitting of the ^{1}H NMRD profiles to the SMB theory, including the Lipari–Szabo approach for internal flexibility

Parameters	GdL_1@AuNPs Value	GdL_2@AuNPs Value
Q	1	1
$\Delta H^{\ddagger}$ [J mol^{-1}]	17	17
k_{ex}^{298} [10^7 s^{-1}]	5.14	5.14
E_R [kJ mol^{-1}] (global)	19.4 ± 1.1	18 ± 3.6
τ_{RH}^{298}[ps] (global)	1900 ± 140	3500 ± 940
E_R [kJ mol^{-1}] (local)	20	18
τ_{RH}^{298}[ps] (local)	460 ± 50	970 ± 230
S^2	0.41 ± 0.04	0.42 ± 0.12
E_V [kJ mol^{-1}]	1	1
τ_V^{298} [ps]	27 ± 4	17± 3
E_H^{298} [10^{-10} m^2 s^{-1}]	23	23
E_{DGH} [kJ mol^{-1}]	20	20
Gd–O [Å]	2.5	2.5
Δ^2 [10^{20} s^{-2}]	0.044 ± 0.002	0.065 ± 0.004
Gd–HW 1st [Å]	3.1	3.1
Gd–HW 2nd [Å]	3.6	3.6

to values determined for the analogous Gd[(DO3A-*N*-(α-benzoylamido)propionate] chelate.[25]

The fittings (continuous lines in Fig. 4) are restricted to frequencies above 6 MHz as the SBM theory is not suitable for describing the rotational dynamics of slow-rotating objects at low magnetic fields. The best fit parameters for Gd$\mathbf{L_1}$@AuNPs and Gd$\mathbf{L_2}$@AuNPs, obtained from the analysis of ^{1}H NMRD data, are presented in Fig. 4 and summarized in Table 2.

The NMRD profiles are characteristics of macromolecular objects in slow rotation, confirming the immobilization of the Gd$\mathbf{L_1}$ and Gd$\mathbf{L_2}$ chelates onto gold nanocrystals: a plateau in the frequency range 0.01 to 1 MHz, a simple dispersion at about 1–10 MHz and a broad hump centered at 20–60 MHz.

The AuNPs prepared in this work display exceptional relaxivities (per Gd^{3+} chelate) (r_{1max} = 27 and 38 mM^{-1} s^{-1} for Gd$\mathbf{L_1}$@AuNPs and Gd$\mathbf{L_2}$@AuNPs, respectively; 30 MHz, 25 °C), much higher than those reported by other authors for AuNPs functionalized with monoaquated (q = 1) Gd^{3+} complexes.[16,19,21] The temperature dependence of the relaxivity, higher relaxivity at lower temperature, for both Gd$\mathbf{L_1}$@AuNPs and Gd$\mathbf{L_2}$@AuNPs, indicates that the water exchange rate is not limiting the relaxivity. The superb relaxivities attained can be ascribed to simultaneous optimization of the water exchange rate (fast water exchange regime) and of the rotational correlation time. The value obtained for the order parameter ($S^2 \sim 0.40$) indicates that fast local motions of the chelates anchored onto the Au core are still limiting the relaxivity. Simulations, using the same parameters as those in Table 3, but assuming total rigidity of the immobilized chelates (S^2 = 1), afford much higher relaxivities (of the order of magnitude 60 mM^{-1} s^{-1}; 20 MHz; 25 °C) for Gd$\mathbf{L_2}$@AuNPs. The higher relaxivity attained by Gd$\mathbf{L_2}$@AuNPs, compared to Gd$\mathbf{L_1}$@AuNPs and Gd$\mathbf{L_3}$@AuNPs, has to be ascribed to its significantly larger global rotational correlation time (τ_{Rg}), reflecting the larger size (hydrodynamic diameter) of the Gd$\mathbf{L_2}$@AuNPs nanoparticles. In fact, the length of the thioalkyl linker seems not to have much influence on the internal flexibility of the immobilized chelates: the order parameter S^2 is identical for Gd$\mathbf{L_1}$@AuNPs and Gd$\mathbf{L_2}$@AuNPs despite the longer linker anchoring Gd$\mathbf{L_2}$ to the Au core. Moreover, the shorter cysteine linker anchoring Gd$\mathbf{L_3}$ to the Au core (possibly in a bidentate (N, S) fashion similar to Gd$\mathbf{L_1}$ (S, S)) results only in slightly higher rigidity of the immobilized chelates. Despite the limiting effect of the internal rotational motions, chelate immobilization onto AuNPs results in relaxivity enhancements of more than 300% for Gd$\mathbf{L_1}$ and over 500% for **Gd**$\mathbf{L_2}$ (compared to its monomeric form), attributed to simultaneous optimization of τ_R and k_{ex}. Moreover, Gd$\mathbf{L_2}$ immobilized onto AuNPs displays a substantially higher relaxivity than the aggregated (micellar) form of Gd$\mathbf{L_2}$ (38 *vs.* 15 mM^{-1} s^{-1}; 20 MHz, 25 °C). The micellar form of the Gd[DO3A-*N*-(α-pyrenebutanamido)propionate] chelate (Gd$\mathbf{L_4}$) (sharing the same coordination cage with Gd$\mathbf{L_{1,2,3}}$) is significantly more flexible (S^2 = 0.24 *vs.* 0.42) than the Au-anchored Gd$\mathbf{L_1}$ and Gd$\mathbf{L_2}$ chelates. Accordingly, Gd$\mathbf{L_2}$@AuNPs, displaying a τ_{Rg} value similar to the aggregated form of Gd$\mathbf{L_4}$, exhibits higher relaxivity (38 *vs.* 32 mM^{-1} s^{-1}; 20 MHz, 25 °C, for Gd$\mathbf{L_2}$@AuNPs and for the aggregated form of Gd$\mathbf{L_4}$, respectively).[26]

Covalent immobilization of Gd^{3+} chelates onto AuNPs seems more effective in attaining high relaxivities than chelate self-assembly into micelle-type structures, owing to higher restriction of internal rotational motions.

Table 3 Selected molecular parameters for Gd$\mathbf{L_1}$@AuNPs and Gd$\mathbf{L_2}$@AuNPs and other systems reported in the literature and discussed in the manuscript

Parameter	GdL_1@AuNPs[a]	GdL_2@AuNPs[a]	GdL_3@AuNPs[b]	GdL_4[c]
Q	1	1	1	1
k_{ex}^{298} [10^7 s^{-1}]	5.14	5.14	5.14	6.2
τ_g^{298} [ps]	1900	3500	2470	3780
τ_{Io}^{298} [ps]	460	970	177	930
S^2	0.41	0.42	0.48	0.24
HD (nm)[d]	4.8	5.9	3.9	49[e]
r_1 (mM^{-1} s^{-1})	27[f,h]	38[f,h]	28[f,h]	32[g,h]
	11.2[f,i]	8.4[f,i]	8.5[f,i]	n.d.

[a] This work. [b] Ref. 27. [c] Ref. 26. [d] From DLS measurements. [e] Z-average from a bimodal distribution of particles. [f] Relaxivity per chelate. [g] Relaxivity of the aggregated form. [h] 20 MHz, 25 °C. [i] 200 MHz, 37 °C.

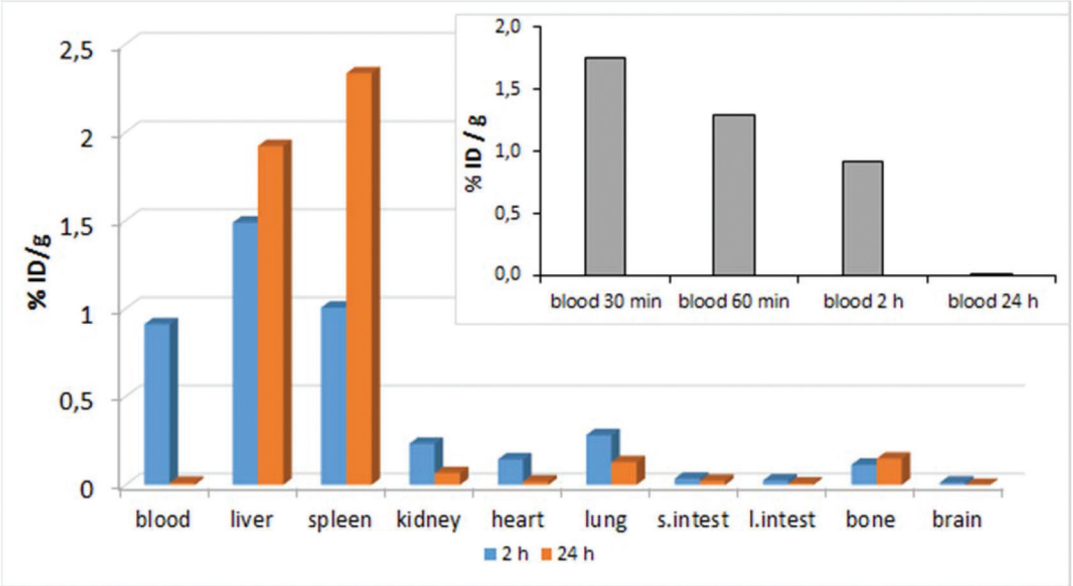

Fig. 5 Biodistribution of $[^{153}Sm^{3+}]L_1$@AuNPs in Wistar rats, stated as percent of injected dose per gram of organ (% ID g^{-1}): (a) 2 and (b) 24 hour post-injection. Inset – time evolution of the activity in the blood. The results are from a group of four animals in each experiment.

The work reported here addresses explicitly the effect of linker length on the relaxivity of AuNPs functionalized with Gd^{3+} chelates, contributing to the "rational design" of nanomaterials as CA for MRI/multimodal imaging.[44]

Biodistribution studies

The biodistribution of $[^{153}Sm]\mathbf{L_1}$@AuNPs in Wistar rats was obtained at 2 and 24 hours post-injection (Fig. 5).

The activity in the blood was measured after 30 minutes, 60 minutes, and 2 and 24 hours (inset in Fig. 5) revealing fast clearance of activity from the blood with a reduction of approximately 50% between 30 minutes and two hours. After 2 hours post-injection, the NPs are mainly found in the organs of the reticulo-endothelial system (RES), liver and spleen, and to a lesser extent in the blood and lungs. These results suggest that the nanoparticles are cleared mainly by phagocytosis by the macrophage rich organs, liver and spleen, with a less important contribution from renal elimination.[20,26,45] This is in accordance with what was found by MRI for Gd$\mathbf{L_1}$@AuNPs (see below).

At 24 hours post-injection significant activity is found only in the organs of the reticulo-endothelial system, RES. The activity approximately doubled in the spleen, showing only a slight increase in the liver. The activity in the bones at 24 hours post-injection is very low, suggesting that the rate of chelate demetallation and formation of insoluble metal colloids *in vivo* is very low.

MRI studies

MRI studies were performed in male Swiss mice (~20 g) in a preclinical imaging platform (PharmaScan) operating at 7.0 Tesla (300 MHz). A Dynamic Contrast Enhancement (DCE) study was performed with Gd$\mathbf{L_1}$@AuNPs (0.1 mmol Gd per kg body weight) and Gd$\mathbf{L_3}$@AuNPs (0.1 and 0.05 mmol Gd per kg body weight) and for comparison purposes with Gd(DTPA) (Magnetvist®, Bayer) at the same doses (Fig. 6). Fig. 6 shows a representative series of T_1-weighted spin-echo coronal images. In the pre-injection images, the kidney structures (cortex, inner and outer medulla) and adjacent tissues appear to be dark. After bolus injection in the vascular system, a strong signal enhancement was observed in the kidneys for Gd(**DTPA**), Gd$\mathbf{L_1}$@AuNPs and Gd$\mathbf{L_3}$@AuNPs as a result of T_1 shortening. A much slighter signal enhancement was observed in the liver. Both NPs follow mainly renal elimination by glomerular filtration, with a significant hepatobiliary contribution to excretion seen for Gd$\mathbf{L_1}$@AuNPs only.

The time course of the average intensity (mean values of groups of four animals) within different regions of interest (ROIs) placed on the several organs (Fig. 7) allows to understand better the features of Fig. 6.

In order to compare the results for all the animals under study (n = 4), the data were normalized by calculating the mean relative enhancement of each ROI. The scattering in the time course curves was caused by animal respiratory motion. The relative enhancement obtained with Gd(**DTPA**) at 0.1 mmol per kg BW dose (Fig. 7A) increased almost immediately after intravenous injection, from 0 up to about 160% in the kidney medulla and 100% in the kidney cortex, followed by a steady decrease to values around 60% and 30%, respectively, within 60 minutes. This time course is in agreement with the literature for the Gd(DTPA) and Gd(DOTA) low molecular weight CA.[46,47]

The enhancement profiles of Gd$\mathbf{L_1}$@AuNPs (Fig. 7B) and Gd$\mathbf{L_3}$@AuNPs (Fig. 7C) at 0.1 mol Gd per kg BW dose are considerably different from the enhancement profile of Gd(**DTPA**) at the same concentration: there is an immediate enhance-

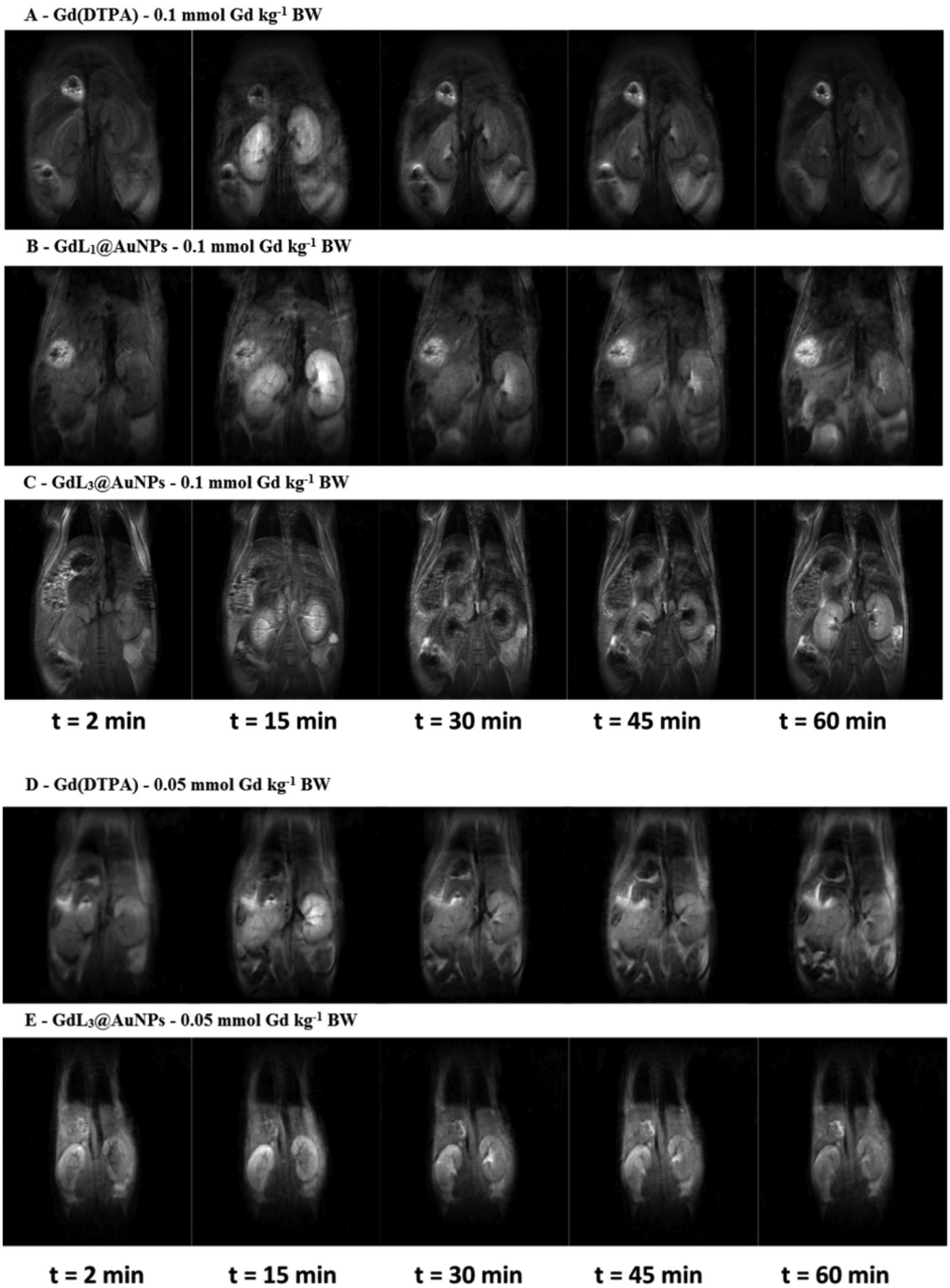

Fig. 6 Representative coronal T_1-weighted spin echo MR images of mice before and after injection of contrast agents: (A) Gd(DTPA) (0.1 mmol Gd per kg BW), (B) Gd**L**$_1$@AuNPs (0.1 mmol Gd per kg BW), (C) Gd**L**$_3$@AuNPs (0.1 mmol Gd per kg BW); (D) Gd(DTPA) (0.05 mmol Gd per kg BW), (E) Gd**L**$_3$@AuNPs (0.05 mmol Gd per kg BW).

ment of the kidney structures (cortex and medulla) followed by a steady liver enhancement. For Gd**L**$_3$@AuNPs at 0.1 mmol Gd per kg BW dose (Fig. 7C), a fast and strong enhancement of the kidney medulla and the kidney cortex (~150%) is noticeable, which slowly decreases to ~100% over the time course of the experiment. A much lower muscle and liver enhancement is also noticeable. Reducing the dose of Gd**L**$_3$@AuNPs to 0.05 mmol Gd per kg BW results in an imaging profile virtually equivalent to Gd(**DTPA**): fast renal elimination with negligible hepatobiliary contribution (Fig. 7D and E for Gd(**DTPA**) and Gd**L**$_3$@AuNPs, respectively). There is a fast enhancement of the kidney cortex (~150% at 20 minutes) which steadily decreases over the time course of the experiment. These results strongly suggest that while Gd**L**$_1$@AuNPs is mostly eliminated through hepatobiliary excretion or is taken up by resident macrophages (Kupfer cells) in liver, Gd**L**$_3$@AuNPs

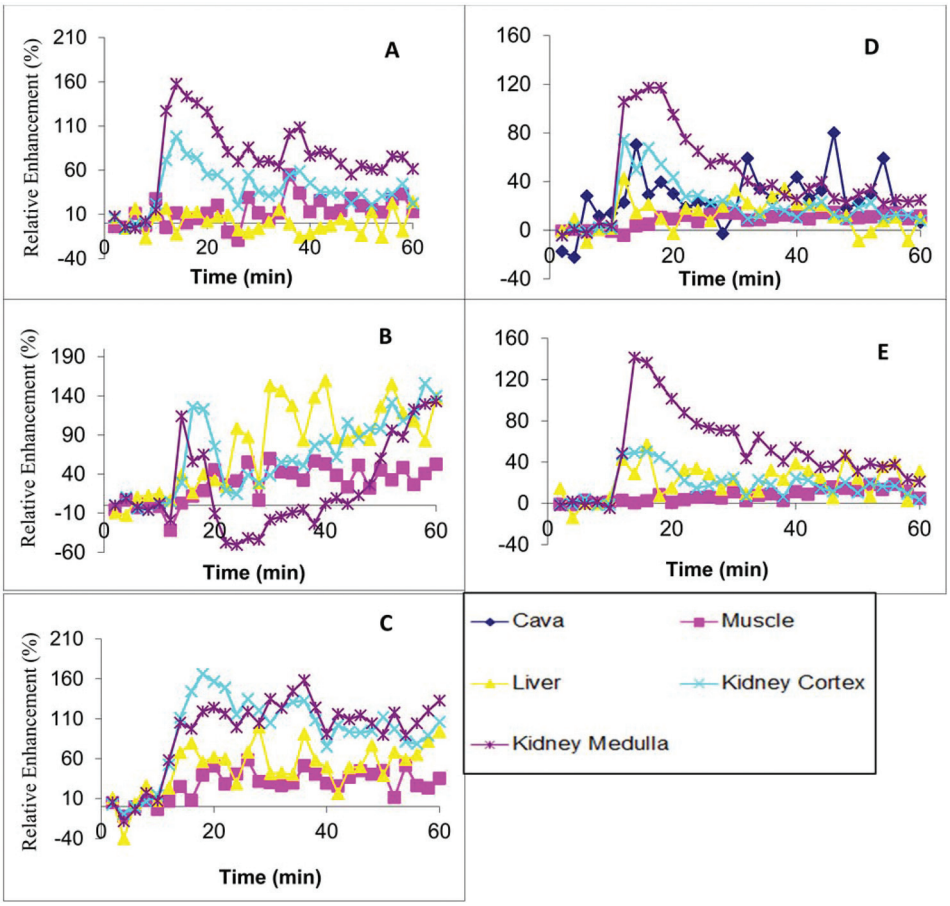

Fig. 7 Time course of signal intensity, up to 60 min post-injection, for several regions of interest, relative to the initial value during dynamic contrast enhancement MRI experiments in rats administrated with: (A) Gd(DTPA) (0.1 mmol per kg BW) and (B) Gd$\mathbf{L_1}$@AuNPs (0.1 mmol per kg BW), (C) Gd$\mathbf{L_3}$@AuNPs (0.1 mmol per kg BW); (D) Gd(DTPA) (0.05 mmol per kg BW); (E) Gd$\mathbf{L_3}$@AuNPs (0.05 mmol per kg BW). The time courses are data from mean values of four animals.

behave *in vivo* as a low molecular weight CA following mainly renal elimination. The steady liver and presumably spleen enhancement observed with Gd$\mathbf{L_1}$@AuNPs is in sharp contrast to the "clean" renal elimination observed for Gd$\mathbf{L_3}$@AuNPs. This behaviour can only be explained by the difference in size between Gd$\mathbf{L_1}$@AuNPs and Gd$\mathbf{L_3}$@AuNPs – average HD 4.8 and 3.9 nm, respectively, stressing the complex interplay between the physical–chemical properties of nanostructures and *in vivo* behaviour.

The animal MRI studies were performed at a high field (300 MHz, 7 Tesla). This study illustrates the mismatch between the performance of macromolecular/nanosized CA, optimized for intermediate fields (20–60 MHz), and the trend for increasingly higher magnetic field images. The overwhelming advantage of the AuNPs over low molecular weight CA at intermediate fields (20–60 MHz) is partially eroded at higher magnetic fields (Fig. 4).[48] Nonetheless, the AuNPs studied in this work still exhibit relaxivities significantly higher than Gd-(**DTPA**) at high fields (11.2, 8.4 *vs.* ~2 mM^{-1} s^{-1} for Gd$\mathbf{L_1}$@AuNPs and Gd$\mathbf{L_2}$@AuNPs, respectively, and Gd(DTPA), 200 MHz, 25 °C).

Conclusions

In this work we extend the synthetic methodologies developed before for AuNPs functionalized with stable fast water exchanging Gd^{3+} chelates as high relaxivity, potentially safe CA for *in vivo* MRI. Two novel ligands were designed to investigate the role of the length of the ω-thioalkyl linker, anchoring the coordination cage to the gold nanocrystal, on the relaxivity. Superb relaxivities at magnetic fields relevant for clinical imaging (27 and 38 mM^{-1} s^{-1}, 30 MHz, 25 °C, for Gd$\mathbf{L_1}$@AuNPs and Gd$\mathbf{L_2}$@AuNPs, respectively) were obtained thanks to simultaneous optimization of the rotational correlation time and of the water exchange rate. Relaxivities, still relevant for clinical high field applications (of the order of magnitude 10 mM^{-1} s^{-1}; 200 MHz, 37 °C), were also attained. The relaxivity is still limited by internal flexibility of the immobilized chelates. The degree of internal flexibility of the immobilized chelates (measured by the order parameter S^2) seems not to be determined by the length of the linker, presumably owing to the high surface curvature of the NPs. An MRI study in mice demonstrated that while Gd$\mathbf{L_3}$@AuNPs

(HD = 3.9 nm) behave *in vivo* much like the low molecular weight CA Gd(**DTPA**), undergoing fast renal elimination without liver (and presumably spleen) uptake, Gd**L$_1$**@AuNPs (HD = 4.8 nm) shows a considerable hepatobiliary contribution to elimination. A biodistribution study in rats using the surrogate ^{153}Sm**L$_1$**@AuNPs tracer confirmed extensive activity uptake and accumulation over time in the liver and spleen.

The Gd**L$_3$**@AuNPs CA, amenable to further elaboration with targeting moieties, seems particularly promising for *in vivo* MRI applications.

The work reported here is a relevant contribution towards the design of nanomaterials functionalized with Gd^{3+} chelates as very high relaxivity/multimodal CA for MRI.[44]

Experimental

Materials and methods

Chemicals were purchased from Sigma-Aldrich and used without further purification. *Cyclen* was purchased from Chematech, France. Analytical grade solvents were used and not further purified, unless specified. Reactions were monitored by TLC on silica gel by examination under UV light (250 and 365 nm) and staining with iodine vapour and Ellman's reagent. Preparative chromatography was carried out on Silica Gel 60 (230–400 mesh). Ion exchange chromatography was performed on Dowex 1X2-100-OH$^-$ (50–100 mesh) resin. Size exclusion chromatography (SEC) was performed on Sephadex G10 (40–120 μm) with water elution. Dialysis was performed against water on cellulose membranes (MWCO 10 kDa). UV-Vis spectra were acquired with a Shimadzu UV-2501PC spectrophotometer. The size distribution and zeta potential of the AuNPs were determined with a Malvern zetasizer, NANO ZS (Malvern Instruments Limited, UK), using a He–Ne laser (wavelength of 633 nm) and a detector angle of 173°. TEM experiments were performed with a JEOL JEM1200EXII microscope at Bath University, UK. Mass spectrometry was performed at CACTI, Vigo, Spain.

^{1}H and ^{13}C NMR spectra were run on Varian Unity Plus 300, Bruker Avance-3 400 Plus and Varian VNMRS 600 NMR spectrometers. Chemical shifts (δ) are given in ppm relative to the $CDCl_3$ solvent (^{1}H, δ 7.27; ^{13}C 77.36) as the internal standard. For ^{1}H and ^{13}C NMR spectra recorded in D_2O, chemical shifts (δ) are given in ppm, relative to TSP as the internal reference (^{1}H, δ 0.0) and *tert*-butanol as the external reference (^{13}C, CH_3 δ 30.29), respectively.

Preparation of lipoic acid conjugate DO$_3$A-*N*-(α-lipoamido)-propionate – L$_1$

Synthesis of ((5-(1,2-dithiolan-3-yl)-2-pentanamido)methoxycarbonylethyl)-4,7,10-tris-(ethoxycarbonylmethyl)-1,4,7,10-tetraazacyclododecane – fully protected conjugate 7. Orthogonally protected compound **6** was synthesized as described before by us.[27] A solution of compound **6** (85 mg; 1.12 mmol) in a DCM–TFA mixture (24 ml, 3 : 1, v/v) was stirred at room overnight. The solvent was removed under reduced pressure, the residue was re-dissolved in DCM and the solvent was evaporated. This procedure was repeated several times.

The resulting oil was dried under vacuum to afford a white foam. ^{1}H NMR ($CDCl_3$) revealed the disappearance of the signals assigned to the Boc groups on compound **6**. Quantitative deprotection was assumed. The residue (1.12 mmol, assuming quantitative deprotection) was dissolved in DCM (20 ml) and the solution was adjusted to pH 9–10 (pH paper) by drop-wise addition of DIPEA. To this solution was added sequentially lipoic acid (288 mg; 1.40 mmol), HOBt (214 mg; 1.40 mmol) and a solution of DCC (288 mg; 1.40 mmol) in DCM (5 ml). The solution was stirred at room temperature overnight. The DCU byproduct was removed by filtration and the reaction mixture was concentrated under reduced pressure. The residue was re-dissolved in ethyl acetate (100 ml), and the solution was washed with $NaHCO_3$ (50 ml, saturated solution) and brine (3 × 50 ml). The organic phase was dried ($MgSO_4$) and concentrated under reduced pressure to afford the title compound (**7**) (358 mg; 44%). ^{1}H NMR (300 MHz, $CDCl_3$): δ = 1.28 (m, 9H, C(O)OCH$_2$C*H*$_3$), 1.48 (m, 2H, NHC(O)-CH$_2$CH$_2$C*H*$_2$), 1.70 (m, 2H, NHC(O)CH$_2$C*H*$_2$), 2.18 (m, 2H, NHC(O)CH$_2$CH$_2$CH$_2$C*H*$_2$), 2.30 (m, 4H, NHC(O)C*H*$_2$ and CHC*H*$_2$CH$_2$S), 2.60–3.60 (broad overlapped signals, integrating for 16H, N(CH$_2$)$_2$N; 2H, *AB*X; 2H, CHCH$_2$C*H*$_2$S, 1H, C*H*SCH$_2$CH$_2$S), 3.73 (m, 6H, C(O)C*H*$_2$N), 3.97 (s, 3H, C(O)-OC*H*$_3$), 4.19 (m, 6H, C(O)C*H*$_2$CH$_3$), 4.90 (dd, 1H, AB*X*). HRMS (ESI): *m*/*z*: calcd for $C_{32}H_{58}N_5O_9S_2$ [M + H]$^+$: 720.3676, found: 720.3645.

Preparation of ((5-(1,2-dithiolan-3-yl)-2-pentanamido)-carboxyethyl)-4,7,10-tris-(carboxymethyl)-1,4,7,10-tetraazacyclododecane – fully deprotected DO3A-*N*-(α-lipoamido)propionate chelator (L$_1$)

Compound (**7**) (2.26 g, 3.15 mmol) was dissolved in a water/ethanol mixture (40 ml, 1/1, v/v). The solution was adjusted to pH ∼ 11 with aqueous NaOH 1 M (pH paper) and was kept under stirring at room temperature overnight. Then, the reaction mixture was adjusted to pH ∼ 7 with hydrochloric acid 1 M (pH paper) and concentrated under reduced pressure. The residue was adsorbed onto silica and purified by flash chromatography (CH_2Cl_2 → CH_2Cl_2/EtOH 1/1 → EtOH → EtOH/H_2O 1/1 → H_2O) to afford a light yellow foam. The final compound (**L$_1$**) was further purified by size exclusion chromatography on Sephadex G10 (0.42 μm) with elution with water. The conductivity of the collected fractions was measured and were also tested by TLC (ethanol/water (1/1), revelation with iodine vapor). The high conductivity fractions (salt) were discarded and the medium/low conductivity fractions showing a signal on the TLC were pooled, concentrated at room temperature and further dried under vacuum to afford the final deprotected compound as a light yellow solid (**L$_1$**) (0.685 g, 35%). ^{1}H NMR (300 MHz, D_2O): δ = 1.46 (m, *J* = 7.8 Hz, 2H, NHC(O)-CH$_2$CH$_2$C*H*$_2$), 1.64–1.72 (m, 6H, NHC(O)CH$_2$C*H*$_2$, NHC(O)-CH$_2$CH$_2$CH$_2$C*H*$_2$, CHC*H*$_2$CH$_2$S), 2.01 (m, 2H, NHC(O)C*H*$_2$), 2.34 (t, *J* = 7.5 Hz, 2H, CHCH$_2$C*H*$_2$S), 2.49 (m, 1H, C*H*SCH$_2$CH$_2$S), 2.10–3.40 (broad overlapped signals integrated

to 16H, 4 × N(CH_2)$_2$N, 6H, 3 × $NCH_2C(O)$ and 2H, *AB*X), 4.49 (m, 1H, AB*X*). ^{13}C NMR (75.4 MHz, D_2O): 25.02 (1C, CH_2), 28.32 (1C, CH_2), 33.93 (1C, CH_2), 35.73 (1C, CH_2), 38.22 (1C, CH_2), 40.46 (2C, 2 × CH_2), 47.81 (3C, 3 × CH_2), 49.46 (1C, CH_2), 51.37 (1C, *C*HCH_2), 51.94 (2C, CH_2), 54.51 (2C, CH_2), 56.08 (2C, CH_2), 56.76 (2C, CH_2), 170.94 (1C, C(O), 176.65 (2C, 2 × C(O), 177.36 (2C, 2 × C(O)). HRMS (ESI): *m*/*z*: calcd for $C_{25}H_{44}N_5O_9S_2$ [M + H]$^+$: 622.2580, found: 622.2572.

Preparation of 11-mercaptoundecanoic acid conjugate DO3A-*N*-(α-mercaptoundecanamido)propionate – L_2

Synthesis of 11-(acetylthio)undecanoic acid (10). To an ice-cooled solution of 11-mercaptoundecanoic acid (**9**) (2.00 g, 9.17 mmol) in pyridine (2.6 ml) was added acetic anhydride (2.6 ml, 2.81 g, 27.5 mmol). The solution was kept under stirring at room temperature overnight. Ice was directly added to the reaction mixture, followed by magnetic stirring until complete melting of the ice. The mixture was extracted with ethyl acetate (3 × 150 ml). The organic phase was washed with brine (3 × 30 ml), dried ($MgSO_4$) and the solvent was removed under reduced pressure. The residue was further dried under vacuum to afford the final compound as an off-white solid (2.12 g, 89%). ^{1}H NMR (400 MHz, $CDCl_3$): δ = 1.27 (s (br), 12H, 6 × CH_2), 1.58–1.52 (m, 2H, SCH_2CH_2), 1.66–1.59 (m, 2H, (CO_2H) CH_2CH_2), 2.32 (s, 3H, $C(O)CH_3$), 2.35 (t, J = 7.2 Hz, 2H, CH_2COOH), 2.86 (t, J = 7.2 Hz, 2H, SCH_2). ^{13}C NMR (100.62 MHz, $CDCl_3$): δ = 24.61 ($C(O)CH_2CH_2$), 28.73 (SCH_2), 28.97, 29.00, 29.10, 29.13, 29.26, 29.32 (overlapped inner CH_2 signals), 29.43 (SCH_2CH_2), 30.59 (CH_3), 33.99 ($C(O)CH_2$), 179.89 (COOH), 196.11 (S*C*(O)Me). HRMS (ESI): *m*/*z*: calcd for $C_{13}H_{24}NaO_3S$ [M + Na]$^+$: 283.1338, found.: 283.1339.

Synthesis of (11-(acetylthio)undecanoyl)serine methyl ester (11). To an ice-cooled solution of compound **10** (2.12 g, 8.14 mmol) in acetonitrile (70 ml) was added HOBt (1.85 g, 8.95 mmol) and a solution of DCC (1.25 g, 8.14 mmol) in acetonitrile (10 ml). The mixture was kept under stirring at the ice bath temperature and, after 15 minutes, L-serine methyl ester hydrochloride (1.27 g, 8.14 mmol) and triethylamine (1.13 ml, 0.82 g, 8.14 mmol) were added. The reaction mixture was kept under stirring at room temperature overnight. The DCU byproduct was removed by filtration and the sample was concentrated under reduced pressure. The residue was re-dissolved in ethyl acetate (100 ml) and the solution was washed sequentially with $KHSO_4$ (1 M, 3 × 50 ml), $NaHCO_3$ (saturated solution, 50 ml) and brine (3 × 50 ml). The organic phase was dried ($MgSO_4$) and concentrated under reduced pressure to afford title compound **11** (2.73 g; 93%). ^{1}H-NMR ($CDCl_3$, 400 MHz): δ = 1.25 (s (br), 12H, 6 × CH_2), 1.52–1.57 (m, 2H, SCH_2CH_2), 1.58–1.65 (m, 2H, $NHC(O)CH_2CH_2$), 2.25 (t, J = 7.2 Hz, 2H, $NHC(O)CH_2$), 2.30 (s, 3H, $SC(O)CH_3$), 2.84 (t, J = 7.2 Hz, 2H, SCH_2), 3.76 (s, 3H, OCH_3), 3.87 (ddd, J = 3.6, 11.2, 29.8 Hz, 1H, CH_aH_bOH), 3.96 (ddd, J = 4.0, 11.0 and 29.8 Hz, 1H, CH_aH_bOH), 4.67–4.63 (m, 1H, CH), 6.62 (s (br), 1H, NH). ^{13}C-NMR ($CDCl_3$, 100.62 MHz): δ = 24.80 ($NHC(O)CH_2CH_2$), 28.67, 28.95, 29.06, 29.09 (overlapped CH_2 signals), 29.17 (SCH_2), 29.25, 29.27 (overlapped CH_2 signals), 29.37 (SCH_2CH_2), 30.55 (SC(O)*Me*), 36.37 ($C(O)CH_2$), 52.54 (OMe), 54.54 (CH), 63.20 (CH_2OH), 171.03 (*C*(O)OMe), 173.78 (NHC(O)), 196.19 (SC(O)).

Synthesis of *N*-(*tert*-butoxycarbonyl),*N*-(11-(acetylthio)undecanoyl) dehydroalanine methyl ester (3). To a solution of compound (**11**) (0.866 g, 2.40 mmol) in dry acetonitrile (15 ml) was sequentially added DMAP (0.081 g, 0.66 mmol) and Boc_2O (1.44 g, 6.6 mmol). The mixture was kept under stirring for 5 days at room temperature. The reaction progress was monitored by ^{1}H NMR. A small volume of reaction mixture was removed, worked-up as described below, and analyzed by ^{1}H NMR by monitoring the disappearance of the signal of the intermediate carbonate ester and the appearance of the alkenic signals at δ = 5.62 and 6.44 ppm. The solid residues were removed by filtration and the sample was concentrated under reduced pressure. The residue was re-dissolved in ethyl acetate (150 ml), and the solution was washed sequentially with $KHSO_4$ (1 M, 3 × 50 ml), $NaHCO_3$ (saturated solution, 50 ml) and brine (3 × 50 cm^3). The organic phase was concentrated under reduced pressure and the residue was purified by flash chromatography (*n*-hexane → *n*-hexane–ethyl acetate (70 : 30)) to afford the title compound as a thick reddish oil (0.445 g, 58%). ^{1}H-NMR ($CDCl_3$, 400 MHz) δ = 1.27 (s (br), 12H, 6 × CH_2), 1.46 (s, 9H, $C(CH_3)_3$), 1.49–1.57 (m, 2H, SCH_2CH_2), 1.65 (m, 2H, $C(O)CH_2CH_2$), 2.32 (s, 3H, $SC(O)CH_3$), 2.86 (t, J = 7.6 Hz, 2H, $NHC(O)CH_2$), 2.93 (t, J = 7.6 Hz, 2H, SCH_2), 3.78 (s, 3H, $C(O)OCH_3$), 5.62 (s, 1H, CCH_aH_b), 6.44 (s, 1H, CCH_aH_b). ^{13}C-NMR ($CDCl_3$, 100.62 MHz): δ = 24.71 (C(O)-CH_2CH_2), 27.40 (SCH_2CH_2), 27.80 (3 × $OCCH_3$), 28.75, 29.05, 29.08, 29.11, 29.35, 29.44 (overlapped CH_2 signals), 29.38 ($C(O)CH_2$), 30.59 ($SC(O)CH_3$), 37.66 (SCH_2), 52.38 ($C(O)OCH_3$), 83.53 ($OCCH_3$), 125.71 (CCH_2), 135.56 (CCH_2), 151.52 (NC(O)O), 163.68 ($C(O)OCH_3$), 175.66 (NC(O)), 196.00 (SC(O)). HRMS (ESI): *m*/*z*: calcd for $C_{22}H_{37}NaO_6S$ [M + Na]$^+$: 466.2234, found: 466.2223.

Synthesis of (11-(acetylthio)-2-*N*-(*tert*-butoxycarbonyl)undecanamido-methoxycarbonylethyl)-1,4,7,10-tetraazacyclododecane – monoalkylated cyclen (5). To a solution of cyclen (0.260 g, 1.5 mmol) in acetonitrile (30 ml) was added K_2CO_3 (0.83 g, 6.0 mmol) and in several portions compound **3** (0.445 g, 1.0 mmol). The suspension was vigorously stirred at room temperature for 4 hours. The suspended solid was removed by filtration and the solvent was evaporated under reduced pressure.

The residue was purified by flash chromatography (CH_2Cl_2 → CH_2Cl_2/EtOH/NH_3/H_2O (70 : 30 : 5 : 5)) to the afford the title compound **5** as a white foam (0.451 g, 73.0%). ^{1}H-NMR ($CDCl_3$, 400 MHz): δ = 1.33 (s (br), 12H, 6 × CH_2), 1.47 (s, 9H, $OC(CH_3)_3$), 1.60 (m, 2H, $C(O)CH_2CH_2$), 1.60–1.65 (m, 2H, SCH_2CH_2), 2.33 (s, 3H, $SC(O)CH_3$), 2.51–2.65 (m, 16H, 4 × N(CH_2)$_2$N), 2.74–2.79 (m, 2H, ($NHC(O)CH_2$)), 2.74–2.79 (m, 1H, NCH_aCH_bCH), 2.85 (t, J = 7.2 Hz, 2H, $CH_3C(O)SCH_2$), 3.45 (dd, J = 5.2 and 14.4 Hz, 1H, NCH_aCH_bCH), 3.68 (s, 3H, $C(O)OCH_3$), 5.46 (t, J = 5.2 Hz, 1H, NCH_2CH). ^{13}C-NMR ($CDCl_3$, 100.62 MHz): δ = 25.01 ($C(O)CH_2CH_2$), 27.90 ($OCCH_3$), 28.75 (SCH_2), 29.05, 29.10, 29.17, 29.37, 29.39, 29.40 (overlapped

CH_2 signals), 29.43 (SCH_2CH_2), 30.58 (SC(O)*Me*), 40.06 (C(O)-CH_2), 46.92 (6 × $NHCH_2$), 51.07 (2 × CH_2NCH_2CH), 52.16 (C(O)O*Me*), 53.56 (NCH_2CH), 58.06 (NCH_2CH), 83.99 (C), 151.96 (NC(O)O), 170.84 (*C*(O)OMe), 175.52 (N(Boc)*C*(O)CH_2), 195.99 (SC(O)). HRMS (ESI): *m*/*z*: calcd for $C_{30}H_{58}N_5O_6S$ $[M + H]^+$: 616.4102, found: 616.4100.

Synthesis of (11-(acetylthio)-2-undecanamido-methoxycarbonylethyl)-4,7,10-tris-(ethoxycarbonylmethyl)-1,4,7,10-tetraazacyclododecane – fully alkylated cyclen (8). A solution of monoalkylated cyclen **5** (0.451 g, 0.87 mmol) in trifluoroacetic acid in dichloromethane (33%, 24 ml) was stirred overnight at room temperature. The solvent was evaporated at reduced pressure and the residue was re-dissolved in dichloromethane. The solvent was evaporated again, and this procedure was repeated several times to give a light thick yellow oil which was further dried under vacuum. ^{1}H NMR spectroscopy ($CDCl_3$) revealed the disappearance of the signal assigned to the Boc group in the precursor compound **5**. The deprotected compound (0.87 mmol, assuming quantitative deprotection) was re-dissolved in MeCN (20 ml), K_2CO_3 (1.17 g, 8.46 mmol) was added and the suspension was left under vigorous stirring at room temperature for 30 minutes. Ethyl bromoacetate (0.29 ml, 2.61 mmol) was added, and the suspension was further stirred for 2 hours. The suspended solids were removed by filtration, the solvent was evaporated under reduce pressure and the residue was purified by flash chromatography (CH_2Cl_2 → CH_2Cl_2/EtOH (7 : 3)) to afford compound **8** (0.218 g, 32%) as a white foam.

^{1}H-NMR ($CDCl_3$, 400 MHz): δ = 1.33 (m, 12H, 6 × CH_2), 1.47 (s, 9H, OC(CH_3)$_3$), 1.60 (m, 2H, C(O)CH_2CH_2), 1.60–1.65 (m, 2H, SCH_2CH_2), 2.32 (s, 3H, SC(O)Me), 2.70–2.90 (m, 16H, 4 × $N(CH_2)_2N$), 2.74–2.79 (m, 2H, (C(O)CH_2)), 2.74–2.79 (m, 1H, NCH_aCH_bCH), 2.85 (t, J = 7.2 Hz, 2H, SCH_2), 3.49 (m, 6H, 3 × C(O)CH_2CH_3 and 1H, NCH_aCH_bCH), 3.72 (s, 3H, C(O)OCH_3), 4.19 (m, 6H, C(O)OCH_2CH_3), 5.46 (t, J = 5.2 Hz, 1H, NCH_2CH). HRMS (ESI): *m*/*z*: calcd for $C_{37}H_{68}N_5O_{10}S$ $[M + H]^+$: 774.4681, found: 774.4684.

Synthesis of (11-mercapto-2-undecanamido-carboxyethyl)-4,7,10-tris-(carboxymethyl)-1,4,7,10-tetraazacyclododecane – fully deprotected DO3A-*N*-(α-mercaptoundecanamido)propionate chelator (L_2). Compound **8** (0.218 g, 0.28 mmol) was dissolved in a mixture of EtOH–H_2O (20 ml, 1 : 1 (v/v)). The solution was adjusted to pH ∼ 10–11 (pH paper) with aqueous NaOH (1 M) and kept under stirring at room temperature overnight. The solution was adjusted to pH ∼ 7 (pH paper) with diluted hydrochloric acid (1 M) and was evaporated at reduced pressure (temperature < 40 °C). The residue was adsorbed onto silica and purified by flash chromatography (CH_2Cl_2 → CH_2Cl_2/EtOH 1/1 → EtOH → EtOH/H_2O 1 : 1 → H_2O) to afford a light yellow foam. The residue was re-dissolved in water and was purified by size exclusion chromatography (Sephadex G10). The relevant fractions were pooled together and the solvent was removed under reduced pressure to give chelator L_2 (0.074 g, 42%). ^{1}H-NMR ($CDCl_3$, 400 MHz): δ = 1.33 (s (br), 10H, 5 × CH_2),1.61 (s (br), 2H, $SCH_2CH_2CH_2$), 1.63 (s (br), 2H, (C(O)CH_2CH_2), 1.72 (s (br), 2H, SCH_2CH_2), 2.33 (s (br), 2H, (C(O)CH_2), 2.58 (t, J = 6.8 Hz, 2H, SCH_2), 2.80 (s (br), 1H, NCH_aH_bCH), 2.80 (s (br), 1H, NCH_aH_bCH), 3.18 (s, 4H, $NCH_2CH_2NCH_2CH$), 3.39–3.36 (m, 4H, $N(CH_2)_2N$), 3.43 (s, 8H, 2 × $N(CH_2)_2N$), 3.76 (s (br), 6H, 3 × NCH_2(C(O)OH), 4.52 (s (br), 1H, C*H*). ^{13}C-NMR ($CDCl_3$, 100.62 MHz): δ = 23.82 (SCH_2), 25.13 (C(O)CH_2CH_2), 27.73 (SCH_2CH_2), 28.11, 28.31, 28.39, 28.52, 28.61 (overlapped CH_2 signals), 33.08 ($SCH_2CH_2CH_2$), 35.84 (C(O)CH_2), 38.51 (NCH_2CH), 48.79 (2 × $NCH_2CH_2NCH_2CH$), 51.20 (CH), 51.62 (2 × $NCH_2CH_2NCH_2CH$), 56.56 (3 × NCH_2(C(O)OH), 56.09 (2 × NCH_2CH_2N), 177.14 (NHC(O)), 177.14 (CH*C*(O)OH), 177.30 (3 × NCH_2*C*(O)OH). HRMS (ESI): *m*/*z*: calcd for $C_{28}H_{51}N_5NaO_9S$ $[M + Na]^+$: 656.3305, found: 656.3300.

Preparation of GdL_1 and GdL_2 complexes for relaxometric measurements

A solution of $GdCl_3$ $6H_2O$ was added drop-wise, under magnetic stirring, to an equimolar solution of L_1 or L_2 (5% excess) while keeping the solution pH around 5.8 (pH meter) by the addition of diluted NaOH. The solution was kept under stirring at room temperature overnight. Then, the solution was adjusted to pH 7.0 with NaOH (0.1 M) and filtered through a 0.2 μm syringe filter. The absence of free Gd^{3+} was confirmed by the xylenol orange test. The final concentration of Gd was determined by ICP-OES following sample digestion with nitric acid.

Preparation of gold nanoparticles functionalized with GdL_1 and GdL_2 chelates

An aqueous solution of the ligand DO3A-*N*-(α-Lipoamido)propionate (L_1) (20.5 mM, 4.53 ml, 0.091 mmol) was added drop-wise under magnetic stirring at room temperature to an aqueous solution of $HAuCl_4$ (58.86 mM, 1.54 ml, 0.091 mmol). During the initial stages of the addition of L_1, the light yellow $HAuCl_4$ solution turned dark orange, fading away in color to light yellow with further addition of the ligand. To the reaction mixture was added, in one aliquot, a freshly prepared aqueous $NaBH_4$ solution (522 mM, 0.179 ml, 0.093 mmol). The reaction mixture turned instantaneously dark brown and was kept under stirring at room temperature for 16 hours. The NPs solution was adjusted to pH ∼ 7 (pH meter) by adding aqueous NaOH (0.1 M) and was filtered through a 0.20 μm PTFE syringe filter. A small volume of solution (1 ml) was kept for further characterization. To the remaining NPs solution (∼5.3 ml) was added slowly a solution of $GdCl_3{\cdot}6H_2O$ in water (303 μM, 0.300 ml, 0.091 mmol) while keeping the solution pH at around 5.5 (pH meter) by adding aqueous NaOH 0.1 M. The NPs solution was kept under stirring at room temperature for 16 hours and was adjusted to pH ∼ 7 with aqueous NaOH (1 M solution). The nanoparticles were purified by size exclusion chromatography (Sephadex G10, 0.42 μm) with elution with water. The entire colored broad band eluting from the column was collected without attempting to fractionate the sample. The nanoparticles were further purified by extensive dialysis against water using a 10 kDa MWCO cellulose membrane. The

xylenol orange test indicated the absence of free Gd^{3+} in the gold nanoparticle preparation.

The same procedure was followed for the preparation of Gd$\mathbf{L_2}$@AuNPs starting from the ligand $\mathbf{L_2}$ (20.5 mg mL^{-1}, 2 ml, 0.0647 mmol) and $HAuCl_4$ (22 mg ml^{-1}, 1 ml, 0.0647 mmol).

The Gd and Au contents of the NP preparations ([Gd] = 0.57 mM and 1.30 mM; [Au]/[Gd] = 1.40 and 0.87 for Gd$\mathbf{L_1}$@AuNPs and Gd$\mathbf{L_2}$@AuNPs, respectively) were determined by ICP-OES analysis following sample digestion with *aqua regia*.

NMRD measurements

The NMD measurements were performed using a StelarSpinmaster FFC NMR relaxometer (0.01–20 MHz) equipped with a VTC90 temperature control unit. At higher fields, the ^1H relaxivity measurements were performed on Bruker Minispecs mq30 (30 MHz), mq40 (40 MHz) and mq60 (60 MHz), as well as Bruker Advance spectrometers connected to 2.35 T, 4.7 T and 9.4 T superconducting magnets. In each case, the temperature was measured by a substitution technique. Variable temperature measurements were performed at 25 and 37 °C. The NMRD profiles were analysed using the Visualiseur/Optimiseur 3.6 program running on a Matlab® 6.5 platform.[49]

Relaxivity studies of pH dependence and Zn^{2+} transmetallation

The transmetallation reaction of the Gd$\mathbf{L_1}$ and Gd$\mathbf{L_2}$ chelates and of the metal chelate-decorated NPs Gd$\mathbf{L_1}$@AuNps and Gd$\mathbf{L_2}$@AuNPs against Zn^{2+} was studied by following the time-dependent decrease of the protonic longitudinal relaxation rate, R_1, (20 MHz, 25 °C) of phosphate-buffered saline solutions (PBS, pH 7.1, 10 mM), containing Gd$\mathbf{L_1}$, Gd$\mathbf{L_2}$, Gd$\mathbf{L_1}$@AuNPs and Gd$\mathbf{L_2}$@AuNPs ([Gd] = 1.0, 1.13, 0.42, 1.33 mM, respectively), before and after adding an equimolar amount of $ZnCl_2$, while vigorously stirring the solutions.

The pH dependence of the relaxivity was measured by adjusting the solution pH with aqueous diluted NaOH (0.1 M) or diluted hydrochloric acid (0.1 M), using a Crison micro TT 2050 pH meter equipped with a Mettler Toledo 422 electrode. A Bruker Minispec mq20 relaxometer was used for all measurements (20 MHz, 25 °C).

MRI studies

Preparation of the Gd$\mathbf{L_1}$@AuNPs and Gd$\mathbf{L_2}$@AuNPs CA solutions for MRI studies. The Gd$\mathbf{L_1}$@AuNPs and Gd$\mathbf{L_2}$@AuNPs CA for the MRI studies were prepared following the procedure described above. The final nanoparticle solutions were freeze-dried and their Gd and Au contents (per mg of solid material) were determined by ICP-OES following digestion with *aqua regia*.

***In vivo* MRI studies.** The experimental protocols were approved by the appropriate institutional review committees and meet the guidelines of their responsible governmental agency. The magnetic resonance imaging (MRI) experiments were all performed on a Bruker Pharmascan platform (Bruker Medical GmbH, Ettlingen, Germany) using a 7.0 T (300 MHz) horizontal-bore superconducting magnet, equipped with a ^1H selective 60 mm birdcage resonator and a Bruker gradient insert with 90 mm diameter (maximum intensity 360 mT m^{-1}). Data were acquired using a Hewlett-Packard console running on Paravision software (Bruker Medical GmbH, Ettlingen, Germany) under a LINUX environment.

All MRI examinations were carried out on mice (n = 4, ~20 g body weight) anaesthetized initially by inhalation in an induction box with O_2 (1 L min^{-1}) containing 3% isoflurane, and maintained during the experiment using a face mask allowing free breathing and 1–2% isoflurane on O_2. Animals were taped down into a holder, to minimize breathing-related motion, and were then placed in a heated probe, which maintained the core body temperature at 37 ± 0.5 °C, monitored by a rectal probe. The physiological state of the animal was monitored throughout the entire experiment by a Biotrig physiological monitor (Bruker Medical GmbH, Ettlingen, Germany), using the respiratory rate and body temperature.

Solutions of Gd$\mathbf{L_1}$@AuNPs and Gd$\mathbf{L_2}$@AuNPs 10 mM in [Gd] were prepared by dissolving the freeze-dried NPs in an appropriate volume of PBS buffer. The solutions were filtered through a 0.2 μm syringe filter before injection. 10 mM Gd-(DTPA) (Magnevist®, Schering, Berlin, Germany) solutions were also prepared. The solutions were injected into the catheterized tail vein as a bolus in 20 s (0.05 and 0.1 mmol Gd per kg body weight) using an infusion pump (Panlab, Barcelona, Spain).

Regional contrast agent uptake was assessed using dynamic contrast enhanced (DCE) MRI. DCE MRI experiments were performed with a series of T_1-weighted spin echo images sequentially acquired over 1 h, before and following the injection of the contrast agent 10 min after the beginning of the study. The acquisition parameters were: TR = 310 ms, TE = 10.58 ms, the number of averages = 2, ten coronal slices, slice thickness = 2 mm, FOV = 5.0 × 5.0 cm, matrix = 256 × 256, 30 repetitions with a total acquisition time of 119 s.

MRI data analysis

Data were analyzed with the public domain software ImageJ (http://rsbweb.nih.gov/ij/). With the aim of comparing the pharmacokinetics obtained from different animals, the data were normalized by calculating the percentage of relative, rather than absolute, enhancement:

$$\mathrm{RE} = \frac{(I - I_0)}{I_0} \times 100$$

where I is the signal intensity at any given time after CA injection and I_0 is the intensity before injection. Pharmacokinetic behaviour was analyzed by calculating the average enhancements within the different regions of interest (ROIs) placed on each one of the following regions: liver, kidney medulla, kidney cortex and muscle.

Biodistribution of radiolabeled nanoparticles

Preparation of [^{153}Sm]$\mathbf{L_1}$@AuNPs chelates for the biodistribution studies. In these studies $^{153}Sm^{3+}$ was used as a radioactive surrogate of Gd^{3+}. [$^{153}SmCl_3$] (1 mCi) was added to a

solution of $\mathbf{L_1}$@AuNPs (5 mg freeze-dried NPs) in sodium acetate buffer (400 μL, 0.4 M, pH 5). The solution was stirred at 80 °C for 5 hours. After that, cold $SmCl_3$ was added to each solution in order to obtain an equimolar Sm^{3+} : chelator ratio. The final solution was heated at 80 °C for 2 hours and left overnight at room temperature. The radiolabeled nanoparticles were purified by size exclusion chromatography using a Sephadex G-10 column eluted with 0.4 M acetate buffer. The whole colored broad band eluting from the column was collected and concentrated by centrifugal filtration (Centricon 10 kDa MWCO membrane, Millipore).

Biodistribution studies

Groups of four animals (Wistar rat males weighing *ca.* 200 g) were anaesthetized with Ketamine (50.0 mg mL^{-1})/chloropromazine (2.5%) (10 : 3) and injected in the femoral vein with *ca.* 100 μCi of [^{153}Sm]$\mathbf{L_1}$@AuNPs and sacrificed 2 and 24 hours later. The major organs were excised, weighed and the tissue radioactivity was measured in a γ well-counter. Blood samples were obtained at appropriate periods of time, weighed and the radioactivity counted.

National regulations for the care and use of laboratory animals were strictly followed in this study.

Semiempirical calculations, molecular modelling and NPs size estimates

All calculations were performed with the Mopac code[50] using the semiempirical model Hamiltonian PM6[51] and the COSMO[52] implicit water solvent model (ε = 74.8 with Gd and Au tesserae radius taken as 0.2 nm). The length of the chelates was estimated from various chelate conformers averaged over several S···O and S···H top–bottom distances within conformers (Fig. SI5†); ascribing an error of 0.1 nm to the estimates seems reasonable for this methodology. The average AuNPs diameter is estimated from the diameter exclusion of the left and right chelates (Table SI2†).

Acknowledgements

This work was financially supported by Fundação para a Ciência e a Tecnologia, Portugal: PhD grant SFRH/BD/63994/2009 to Miguel Ferreira and Sabbatical Grant SFRH/BSAB/1328/2013 to José Martins at Bath University, UK; and Rede Nacional de NMR (REDE/1517/RMN/2005) for the acquisition of the Varian VNMRS 600 NMR spectrometer in Coimbra. T.B.R. was supported by a Marie Curie Fellowship (FP/-PEOPLE-2009-IEF 254380) and an EMBO Fellowship (ALTF 1145-2009). Financial support from Ministerio de Ciencia e Innovación, Spain, projects SAF2011-23622 (S.C.) and CTQ2010-20960-C02-02 (P.L.-L.), and Comunidad de Madrid, Spain, project S2010/BMD-2349 (S.C. and P.L.-L), is also acknowledged. B. Mousavi and L. Helm acknowledge financial support by the Swiss National Science Foundation. This work was carried out in the framework of the COST D38 Action "Metal Based Systems for Molecular Imaging" and COST TD1004 Action "Theranostics Imaging and Therapy".

References

1 M. L. James and S. S. Gambhir, *Physiol. Rev.*, 2012, **92**, 897–965.
2 G. J. Stanisz, E. E. Odrobina, J. Pun, M. Escaravage, S. J. Graham, M. J. Bronskill and R. M. Henkelman, *Magn. Reson. Med.*, 2005, **54**, 507–512.
3 S. Laus, R. Ruloff, E. Toth and A. E. Merbach, *Chem. – Eur. J.*, 2003, **9**, 3555–3566.
4 P. Caravan, J. J. Ellison, T. J. McMurry and R. B. Lauffer, *Chem. Rev.*, 1999, **99**, 2293–2352.
5 E. M. Gale, S. Mukherjee, C. Liu, G. S. Loving and P. Caravan, *Inorg. Chem.*, 2014, **53**, 10748–10761.
6 E. Tanimoto, S. Karasawa, S. Ueki, N. Nitta, I. Aoki and N. Koga, *RSC Adv.*, 2013, **3**, 3531–3534.
7 B.-T. Doan, S. Meme and J.-C. Beloeil, in *The Chemistry of Contrast Agents in Medical Magnetic Resonance Imaging*, John Wiley & Sons Ltd, 2013, pp. 1–23.
8 G. J. Strijkers, W. J. Mulder, G. A. van Tilborg and K. Nicolay, *Anti-cancer Agents Med. Chem.*, 2007, **7**, 291–305.
9 Y. X. Wang, *Quant. Imaging Med. Surgery*, 2011, **1**, 35–40.
10 Z. Zhou and Z. R. Lu, *Wiley Interdiscip. Rev.: Nanomed. Nanobiotechnol.*, 2013, **5**, 1–18.
11 J. E. Rosen, S. Yoffe, A. Meerasa, M. Verma and F. X. Gu, *J. Nanomed. Nanotechnol.*, 2011, **2**, 115.
12 X. Ding, C. H. Liow, M. Zhang, R. Huang, C. Li, H. Shen, M. Liu, Y. Zou, N. Gao, Z. Zhang, Y. Li, Q. Wang, S. Li and J. Jiang, *J. Am. Chem. Soc.*, 2014, **136**, 15684–15693.
13 D. K. Chatterjee, P. Diagaradjane and S. Krishnan, *Ther. Delivery*, 2011, **2**, 1001–1014.
14 N. Khlebtsov and L. Dykman, *Chem. Soc. Rev.*, 2011, **40**, 1647–1671.
15 Y. Zhang, W. Chu, A. Foroushani, H. Wang, D. Li, J. Liu, C. Barrow, X. Wang and W. Yang, *Materials*, 2014, **7**, 5169–5201.
16 C. Alric, J. Taleb, G. L. Duc, C. Mandon, C. Billotey, A. L. Meur-Herland, T. Brochard, F. Vocanson, M. Janier, P. Perriat, S. Roux and O. Tillement, *J. Am. Chem. Soc.*, 2008, **130**, 5908–5915.
17 P. J. Debouttière, S. Roux, F. Vocanson, C. Billotey, O. Beuf, A. Favre-Réguillon, Y. Lin, S. Pellet-Rostaing, R. Lamartine, P. Perriat and O. Tillement, *Adv. Funct. Mater.*, 2006, **16**, 2330–2339.
18 J. A. Park, P. A. N. Reddy, H. K. Kim, I. S. Kim, G. C. Kim, Y. Chang and T. J. Kim, *Bioorg. Med. Chem. Lett.*, 2008, **18**, 6135–6137.
19 M. Marradi, D. Alcantara, J. M. de la Fuente, M. L. Garcia-Martin, S. Cerdan and S. Penades, *Chem. Commun.*, 2009, 3922–3924.
20 I. Miladi, C. Alric, S. Dufort, P. Mowat, A. Dutour, C. Mandon, G. Laurent, E. Bräuer-Krisch, N. Herath, J.-L. Coll, M. Dutreix, F. Lux, R. Bazzi, C. Billotey, M. Janier,

P. Perriat, G. Le Duc, S. Roux and O. Tillement, *Small*, 2014, **10**, 1116–1124.
21 M. F. Warsi, R. W. Adams, S. B. Duckett and V. Chechik, *Chem. Commun.*, 2010, **46**, 451–453.
22 M. F. Warsi and V. Chechik, *Phys. Chem. Chem. Phys.*, 2011, **13**, 9812–9817.
23 L. c. Moriggi, C. Cannizzo, E. Dumas, C. d. R. Mayer, A. Ulianov and L. Helm, *J. Am. Chem. Soc.*, 2009, **131**, 10828–10829.
24 M. F. Ferreira, A. F. Martins, J. A. Martins, P. M. Ferreira, E. Toth and C. Geraldes, *Chem. Commun.*, 2009, 6475–6477.
25 M. F. Ferreira, A. F. Martins, C. I. O. Martins, P. M. Ferreira, É. Tóth, T. B. Rodrigues, D. Calle, S. Cerdan, P. López-Larrubia, J. A. Martins and C. F. G. C. Geraldes, *Contrast Media Mol. Imaging*, 2013, **8**, 40–49.
26 M. F. Ferreira, G. Pereira, A. F. Martins, C. I. O. Martins, M. I. M. Prata, S. Petoud, E. Toth, P. M. T. Ferreira, J. A. Martins and C. F. G. C. Geraldes, *Dalton Trans.*, 2014, **43**, 3162–3173.
27 M. F. Ferreira, B. Mousavi, P. M. Ferreira, C. I. O. Martins, L. Helm, J. A. Martins and C. F. G. C. Geraldes, *Dalton Trans.*, 2012, **41**, 5472–5475.
28 S. Torres, J. A. Martins, J. P. André, C. F. G. C. Geraldes, A. E. Merbach and É. Tóth, *Chem. – Eur. J.*, 2006, **12**, 940–948.
29 R. Wei, L. Cheng, M. Zheng, R. Cheng, F. Meng, C. Deng and Z. Zhong, *Biomacromolecules*, 2012, **13**, 2429–2438.
30 P. M. T. Ferreira, H. L. S. Maia, L. S. Monteiro and J. Sacramento, *J. Chem. Soc., Perkin Trans. 1*, 1999, 3697–3703.
31 G. Nicolle, É. Tóth, K.-P. Eisenwiener, H. Mäcke and A. Merbach, *J. Biol. Inorg. Chem*, 2002, **7**, 757–769.
32 J. P. André, É. Tóth, H. Fischer, A. Seelig, H. R. Mäcke and A. E. Merbach, *Chem. – Eur. J.*, 1999, **5**, 2977–2983.
33 S. Laurent, L. Vander Elst, C. Henoumont and R. N. Muller, *Contrast Media Mol. Imaging*, 2010, **5**, 305–308.
34 M. Brust, M. Walker, D. Bethell, D. J. Schiffrin and R. Whyman, *J. Chem. Soc., Chem. Commun.*, 1994, 801–802.
35 A. Barge, G. Cravotto, E. Gianolio and F. Fedeli, *Contrast Media Mol. Imaging*, 2006, **1**, 184–188.
36 D. M. Corsi, C. Platas-Iglesias, H. v. Bekkum and J. A. Peters, *Magn. Reson. Chem.*, 2001, **39**, 723–726.
37 H. Hinterwirth, S. Kappel, T. Waitz, T. Prohaska, W. Lindner and M. Lämmerhofer, *ACS Nano*, 2013, **7**, 1129–1136.
38 M.-C. Daniel and D. Astruc, *Chem. Rev.*, 2003, **104**, 293–346.
39 P. J. Krommenhoek, J. Wang, N. Hentz, A. C. Johnston-Peck, K. A. Kozek, G. Kalyuzhny and J. B. Tracy, *ACS Nano*, **6**, 4903–4911. Q7
40 M. Port, J.-M. Idée, C. Medina, C. Robic, M. Sabatou and C. Corot, *BioMetals*, 2008, **21**, 469–490.
41 K. Kumar, C. A. Chang and M. F. Tweedle, *Inorg. Chem.*, 1993, **32**, 587–593.
42 A. Borel, J. F. Bean, R. B. Clarkson, L. Helm, L. Moriggi, A. D. Sherry and M. Woods, *Chem. – Eur. J.*, 2008, **14**, 2658–2667.
43 F. A. Dunand, É. Tóth, R. Hollister and A. E. Merbach, *J. Biol. Inorg. Chem.*, 2001, **6**, 247–255.
44 G. J. Stasiuk, S. Tamang, D. Imbert, C. Gateau, P. Reiss, P. Fries and M. Mazzanti, *Dalton Trans.*, 2013, 8197–8200.
45 S. Torres, M. I. M. Prata, A. C. Santos, J. P. André, J. A. Martins, L. Helm, É. Tóth, M. L. García-Martín, T. B. Rodrigues, P. López-Larrubia, S. Cerdán and C. F. G. C. Geraldes, *NMR Biomed.*, 2008, **21**, 322–336.
46 N. Raghunand, C. Howison, A. D. Sherry, S. Zhang and R. J. Gillies, *Magn. Reson. Med.*, 2003, **49**, 249–257.
47 D. Baumann and M. Rudin, *Magn. Reson. Imaging*, 2000, **18**, 587–595.
48 L. Helm, *Future Med. Chem.*, 2010, **2**, 385–396.
49 F. Yerly, VISUALISEUR/OPTIMISEUR, EPFL, 2003.
50 MOPAC2012J. J. P. Stewart, *Stewart Computational Chemistry*, Colorado Springs, CO, USA, 2012, http://OpenMOPAC.net.
51 J. P. Stewart, *J. Mol. Model.*, 2007, **13**, 1173–1213.
52 A. Klamt and G. Schuurmann, *J. Chem. Soc., Perkin Trans. 2*, 1993, 799–805.

